Chapter 4

Synthesis, mechanical, electrical, polarization induced antibacterial and cellular response of HA - NKN composite

Among various calcium phosphate bioceramics, hydroxyapatite (HA) possesses similar chemical as well as crystallographic properties to that of the inorganic component of the natural bone [1]. HA is extensively used for orthopedic implantation such as in bone fixation, bone screws etc [2]. HA has been reported to enhance the interaction with the host bone tissue with the exchange of its calcium and phosphate ions [3,4]. Therefore, HA has been regarded as an excellent biocompatibilty material [5 – 8]. Besides remarkable potential of HA as for orthopedic applications, poor mechanical and electrical response as well as susceptibilities towards bacterial infection limit it's widespread applications. In order to overcome above mentioned limitations, this chapter discusses the effects of incorporation of varying amounts of piezoelectric NKN secondary phase in HA on mechanical, dielectric, electrical, polarization induced antibacterial as well as cellular response of HA – NKN composite system.

4.1. Particle size and density measurement

The average particle size for ball milled HA, NKN, HA – 10 wt. % NKN (HA – 10 NKN), HA - 20 wt. % NKN (HA – 20 NKN) and HA – 30 wt. % NKN (HA – 30 NKN) powder samples was obtained to be 128 nm, 50 nm, 150 nm, 152 nm and 175 nm, respectively.

Fig. 4.1 represents the comparison of the relative sintered density of samples, processed using uniaxial and cold isostatical (CIP) pressings. CIPed samples are observed to possess higher densification than those of uniaxial pressed samples. With CIP, more than 95% densification of their respective theoretical densities has been achieved.

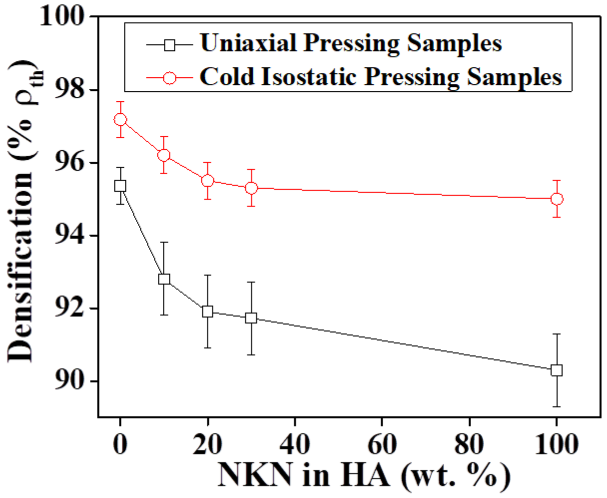

Fig. 4.1. Densification behavior for HA, NKN and HA – (10 – 30) NKN composites, synthesized using uniaxial as well as cold isostatic pressings (CIP).

4.2. XRD Analysis

X-ray diffraction patterns reveal the formation of single phase HA (# 09-0432) and NKN (#77-0038) [Fig. 4.2]. HA and NKN are indexed for the hexagonal and monoclinic structures, respectively using X'Pert highscore and JCPDS data. All the XRD peaks of the HA- xNKN composites are indexed for HA and NKN phases only. Any signature of dissociation of HA and NKN or reaction between HA and NKN phases in the HA-xNKN composite were not observed using the optimal processing parameters (compacted at 300 MPa and sintered at 1075ºC for 2 h).

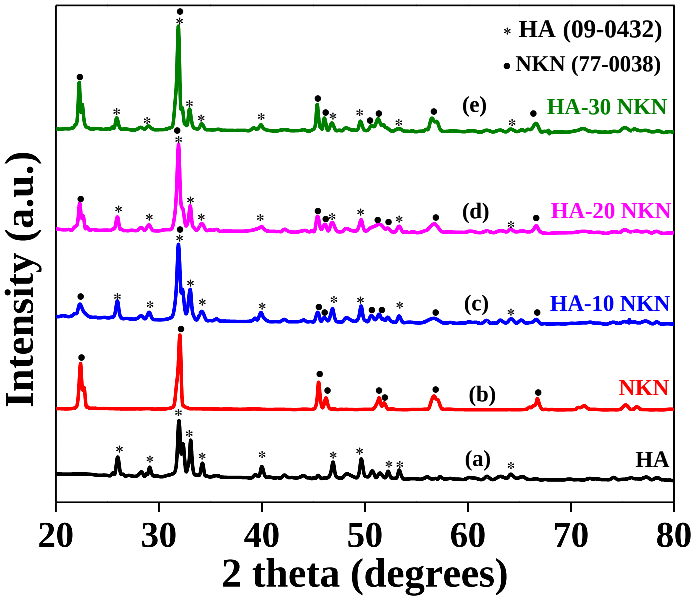

Fig. 4.2. X-Ray diffraction patterns for HA, NKN and HA – (10 – 30) NKN composite samples.

4.3. Fourier Transform Infrared Spectroscopic analysis

Fig. 4.3 represents the FTIR spectra of the sintered monolithic HA and HA – (10 – 30) NKN composite samples. HA shows a characteristic bands, corresponding to hydroxyl groups (OH^-) at 3572 cm^{-1} and 630 cm^{-1} and phosphate groups (PO_4^{3-}) at 563, 599, 962, 1026 and 1089 cm^{-1}, indicating the formation of phase pure HA [9] [Fig. 4.3 (a)]. FTIR spectra reveal the peak of NbO at 524 cm^{-1}, suggesting the formation of NKN phase [Fig. 4.3 (b)] [10] HA – (10 – 30) NKN composites show the peaks of OH^-, PO_4^{3-} and Nb=O without any deviation with monolithic HA and NKN phases [Figs. 4.3 (c-e)].

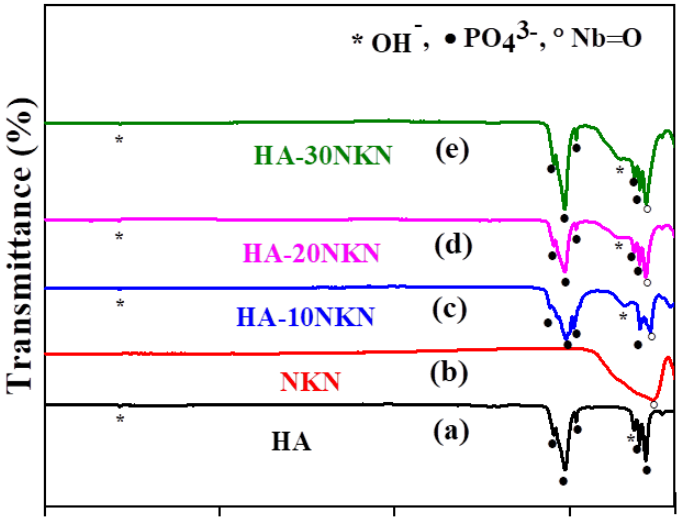

Fig. 4.3 Fourier transform infra-red (FTIR) spectra for HA, NKN and HA – (10 – 30) NKN composite samples.

4.4 Scanning electron microscope

Fig. 4.4 shows the SEM images for the microstructure of fractured surfaces of HA, HA – (10 – 30) NKN composites. For grain size measurement, image j software was used. The distribution of grains were found to be similar for all the composites. The variation of grain size for HA, HA – 10 NKN, HA – 20NKN and HA – 30 NKN compoistes were observed to be in the range of 0.5 – 0.7 µm, 0.5 – 0.75 µm, 0.5 – 0.8 µm and 0.4 – 0.9 µm.

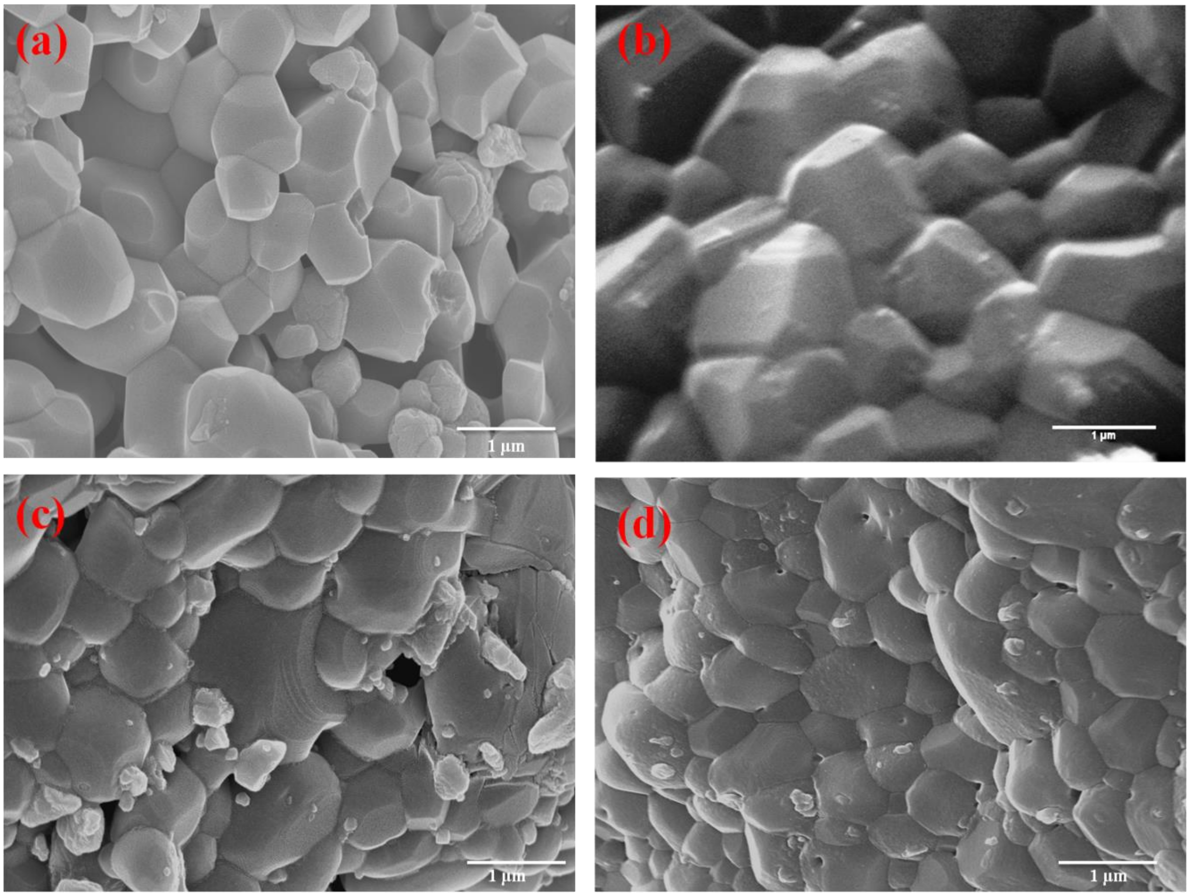

Fig. 4.4 SEM micrographs of (a) HA, (b) HA – 10 NKN, (c) HA – 20 NKN and (d) HA – 30 NKN composites

4.5. Mechanical behavior

4.5.1. Hardness and fracture toughness

Vickers hardness and indentation fracture toughness were calculated for the monolithic HA and HA - (10 – 30) NKN composite samples [Fig. 4.5 (a)]. Hardness of the sintered HA - (10 – 30) NKN composite samples relatively vary over the range of (5.08 ± 0.25) to (7.90 ± 1.03) GPa, whereas, the hardness value for monolithic HA was obtained to be (4.10 ± 0.25) GPa. Zysset et al.[11] reported the hardness value for natural bone to be about 1 GPa. It has been observed that the incorporation of piezoelectric NKN in HA enhances the hardness of the HA – (10 – 30) NKN composite samples. The values of indentation fracture toughness for the sintered composite samples vary from 0.59 ± 0.11 to 1.03 ± 0.15 MPa.$m^{1/2}$ whereas the monolithic HA exhibited fracture toughness value of 0.42 ± 0.13 MPa.$m^{1/2}$. The fracture toughness of the fabricated composite samples requires further improvement for the purpose of load bearing applications. The fracture toughness of the natural bone has been reported to be 2 – 12 MPa.$m^{1/2}$. [11]

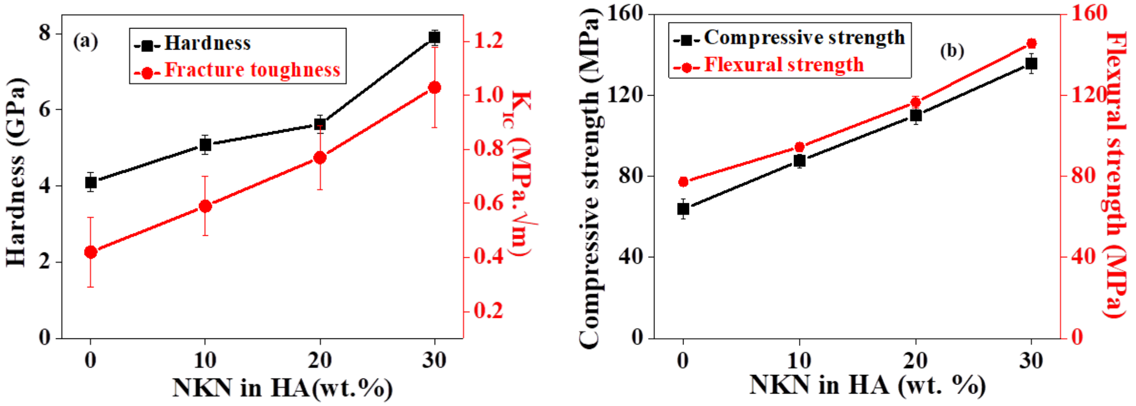

Fig.4.5. Variation of mechanical properties of HA with addition of NKN (a) Hardness and fracture toughness, (b) Compressive strength and flexural strength

It is observed that the fracture toughness of HA is enhances by the addition of piezoelectric NKN as the secondary phase. HA – 30 NKN composite shows the maximum value of fracture toughness (~ 1.3 ± 0.15 MPa.$m^{1/2}$). It has been suggested that the addition of piezoelectric secondary phase in the matrix provide the additional toughening via domain switching and other energy dissipation mechanisms where some of crack energy is utilized in the process of dipole alignment and domain wall motion [12]. At the same time, it is observed that the addition of secondary phase toughens the ceramics by various toughening mechanisms such as crack deflection, crack bridging etc. Fig. 4.6 represents the SEM images of fractured surfaces which indicate the crack deflection and thereby increasing the crack length.

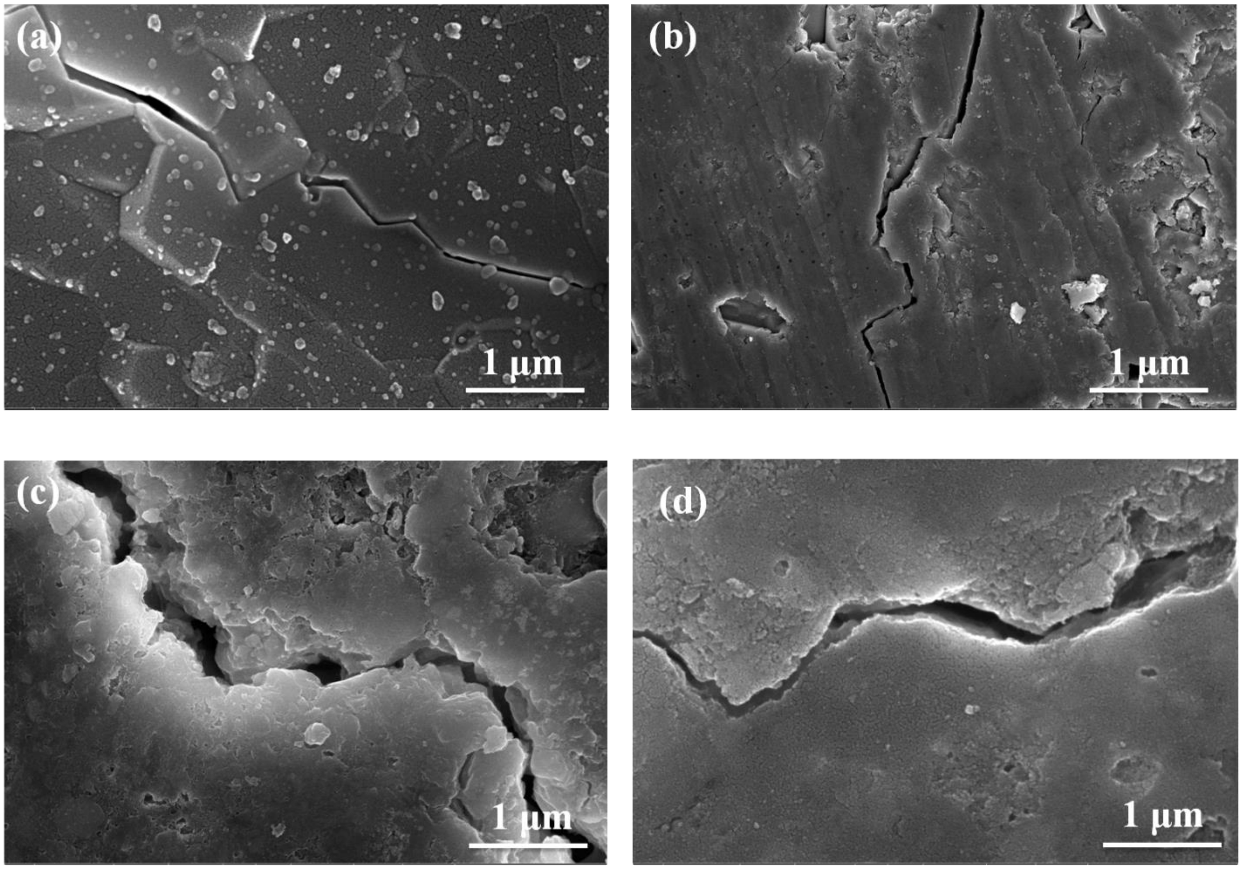

Fig. 4.6 SEM micrographs revealing crack deflection for (a) monolithic HA, (b) HA – 10 NKN, (c) HA – 20 NKN and (d) HA – 30 NKN composites after indentation fracture

Overall, the incorporation of piezoelectric NKN secondary phase in HA enhances the hardness and fracture toughness of HA – NKN composite significantly.

4.5.2. Compressive and flexural strength

Fig. 4.5 (b) represents the variation of compressive and flexural strengths for monolithic HA and HA - (10 - 30) NKN composite system. The values of compressive strength of the fabricated HA- (10 - 30) NKN composite samples have been observed to vary from 87.55 to 135.62 MPa whereas the monolithic HA exhibits a low value of compressive strength (63.84

MPa). For natural bone, the value of compressive strength along the bone axis has been reported to be 131 MPa [13,14]. It is observed that the addition of piezoelectric NKN as the secondary phase (30 wt. %) in HA enhances the compressive strength by almost 113% than that of monolithic HA, which is comparable to natural bone. Flexural strength of the sintered composite has been enhanced from 94.53 to 145.52 MPa after the addition of piezoelectric NKN secondary phase in HA which is almost 88 % more than that of the monolithic HA (77.21 MPa) [Fig. 4.5 (b)]. The flexural strength of natural cortical bone has been reported to be about 160 MPa [15,16]. The addition of piezoelectric material as the secondary phase in the matrix provides the additional strengthening to the material by dissipating the crack energy and domain wall motion [12].

4.6 Dielectric measurement

Fig. 4.7 shows the variation of dielectric constant and loss with temperature for HA, NKN, HA – (10 – 30) NKN composites at selected frequencies of 10 kHz, 100 kHz and 1 MHz, respectively. The dielectric constant of HA and HA – (10 – 30) NKN composites increases with temperature at a particular frequency, after a plateau region in low temperature range of up to 200ºC [Figs. 4.7 (a - e)]. In case of NKN, the peaks in curve, represent transition temperatures of NKN [Fig. 4.7 (b)]. The first transition peak is observed to occur at about 190^{o}C where crystal structure of NKN changes from orthorhombic to tetragonal phase and other at about 400^{o}C where transition occurs from tetragonal to cubic structure [17]. At transition points, abrupt variation in dielectric constant is observed. At room temperature, the dielectric constant and loss for HA, NKN and [HA – (10 - 30) NKN] are observed to be (25.23, 0.33), (307.94, 0.14), (17.89, 0.11), (14.12, 0.10) and (17.67, 0.08), respectively measured at 10 kHz. The variation of dielectric constant with temperature is due to relaxation of space charge and dipolar polarizations [18]. The interfacial polarization, due to presence of the phases with different electrical conductivity is one of the reasons for the variation in dielectric properties [8].

The dielectric constant decreases with increase in frequency [Fig. 4.8]. For lower frequencies (1 – 100 Hz), the variation in dielectric behavior, above 200°C represents the relaxation of interfacial or space charge polarization. At very low frequencies (1- 10 Hz), the dielectric constant increases prominently as the operating temperature increases. Such variation in dielectric constant became insignificant at higher frequency (~ 1 MHz) [Fig. 4.8].

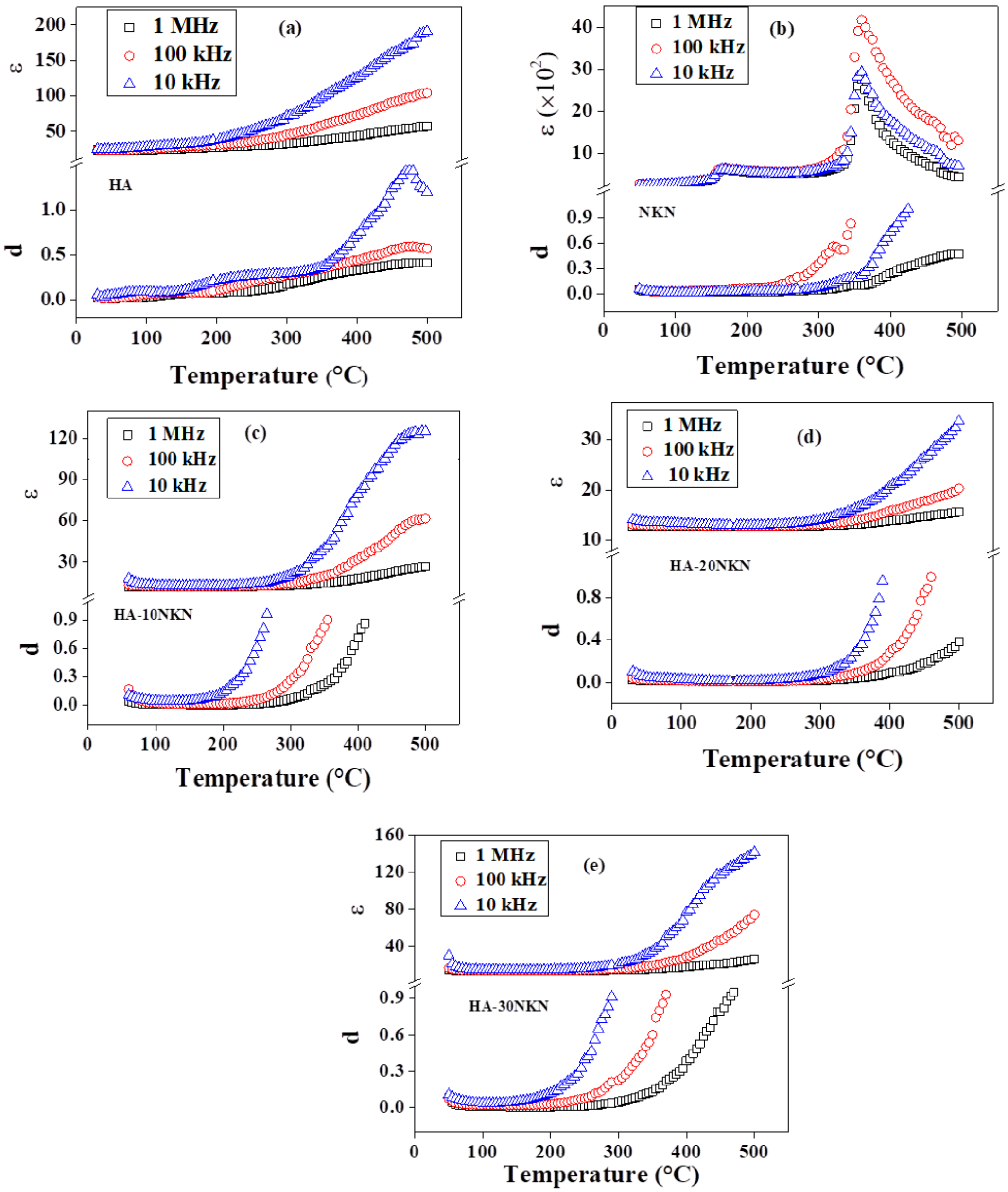

Fig .4.7 Variation of dielectric constant and loss with temperature at few selected frequencies for (a) HA, (b) NKN, (c) HA-10 NKN, (d) HA-20 NKN and (e) HA-30 NKN composites.

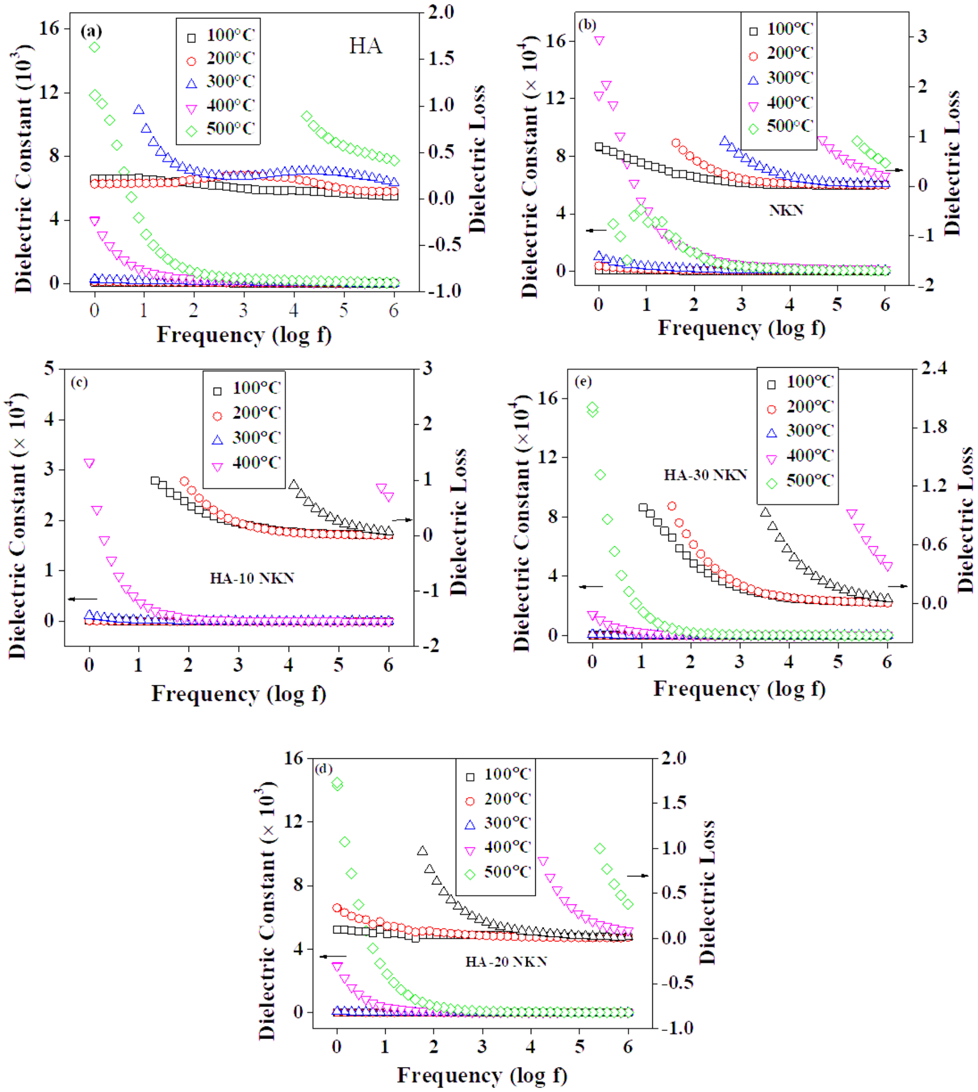

Fig. 4.8 Variation of dielectric constant and loss with frequency for (a) HA, (b) NKN, (c) HA-10 NKN, (d) HA-20 NKN and (e) HA-30 NKN

HA possesses the hexagonal crystal structure in which OH^- ions exist at centroid of the triangle, formed by Ca^{2+} ions along the longitudinal axis of hexagonal unit cell together with tetrahedral phosphate (PO_4^{3-}) ions [19]. The polarization mechanism in HA is governed by dipolar arrangement of OH^- ions, present along c- axis of hexagonal HA [20]. For the given temperature and frequency, the orientation of OH^- ions (dipole) is an influential factor in dielectric behavior [21]. The phase change of HA occurs due to the temperature induced orientation of hydroxyl ions (OH^-) [22]. The dielectric behavior of HA at lower temperature is related with the structural defects like, vacancy as well as O^- and OH^- ions as [23],

$$\mathbf{Ca_{10}(PO_4)_6(OH)_2 \rightarrow Ca_{10}(PO_4)_6O\,\square + H_2O} \tag{4.1}$$

(Where, symbol $\square$ represents a vacancy)

It has been reported that the dehydration of OH^- ions in HA is one of the responsible factors for observed dielectric behavior at high temperature [24]. Horiuchi et al. [21] reported that the dielectric behavior of HA are influenced by polarization which is thermally activated process because of presence of OH^- ions.

During sintering of NKN, volatilization of alkali metals (sodium and potassium) occurs which can be expressed as [25],

$$\mathbf{2\,M_M^{\times} + O_O^{\times} \leftrightarrow M_2O \uparrow + 2\,V_M' + V_O^{\circ\circ}} \tag{4.2}$$

During the cooling of the samples in air atmosphere, ionic to electronic p-type conduction (via holes) occurs mainly in grain boundary area due to superoxidation process as [25],

$$\mathbf{2\,V_M' + V_O^{\circ\circ} + \frac{1}{2}O_2 \leftrightarrow 2\,V_M' + O_O^{\times} + 2\,h^{\circ}} \tag{4.3}$$

Therefore, p-type conduction is the dominating conduction mechanism which occurs during sintering of alkali niobate as [25],

$$\mathbf{2\,M_M^{\times} + \tfrac{1}{2}O_2(gas) \leftrightarrow M_2O(gas) + 2\,V_M' + 2\,h^{\circ}} \tag{4.4}$$

Where, M denotes the alkali metal, V and h denote the vacancy and hole, respectively. P type conductivity (generation of intrinsic vacancies of K and Na) decreases in low oxygen partial pressure (pO_2) atmosphere because it reduces the volatilization of alkali metals. Owing to the generation of O_2 vacancies at low pO_2, samples show **n** type conductivity [25],

$$\mathbf{O_O^{\times} \rightarrow \frac{1}{2}O_2 + V_O^{\circ\circ} + 2\,e'} \qquad \textbf{(4.5)}$$

The measured dielectric constant values have been compared with those of the calculated from existing theoretical models. Dielectric constant of HA-10 NKN, HA - 20 NKN and HA-30 NKN composites were calculated by the parallel and series Wiener bounds [26] as well as logarithmic mixture rule as, [27]

$$\boldsymbol{\varepsilon_{composite} = V_{HA}\varepsilon_{HA} + V_{NKN}\varepsilon_{NKN}} \qquad (\mathbf{4.6})$$

$$\boldsymbol{\frac{1}{\varepsilon_{composite}} = \frac{V_{HA}}{\varepsilon_{HA}} + \frac{V_{NKN}}{\varepsilon_{NKN}}} \qquad (\mathbf{4.7})$$

$$\boldsymbol{\log \varepsilon_{\tau} = \Sigma_i V_i \log \varepsilon_i} \qquad \textbf{(4.8)}$$

Where, V is volume fraction of corresponding phase and ε is dielectric constant.

As can be seen from Fig. 4.9 that the experimental values are lower than those of the calculated values, using the above theoretical models. One of the reasons for this deviation is the connectivity between HA and NKN phases, especially for the lower content of NKN in HA matrix. The connectivity between matrix and secondary phase influence the electrical as well as mechanical properties of the composites [28]. For lower content of NKN, it is possible that HA phases are connected in 3- dimension and there is no connectivity between NKN phases i.e., there is 0-3 connectivity between NKN and HA phases. Landauer expression for 0-3 connectivity of the binary systems can be given as [29]

$$\boldsymbol{F = V_1\frac{\varepsilon_1 - \varepsilon_c}{\varepsilon_1 + 2\,\varepsilon_c} + V_2\frac{\varepsilon_2 - \varepsilon_c}{\varepsilon_2 + 2\,\varepsilon_c}} \qquad (\mathbf{4.9})$$

Where, V_1 and V_2 are the volume fractions of the constituent phases. ε_1, ε_2 and ε_c are the dielectric constant of secondary phase, matrix and composites, respectively. From eq. 4.9, the calculated values of F for HA – 10 NKN, HA – 20 NKN and HA – 30 NKN at 10 kHz were 0.17, 0.31 and 0.29, respectively. For perfect 0-3 connectivity, the value of F should be zero [29]. With increasing content of NKN phases in HA matrix, the interaction between piezoelectric phases is suggested to increase and dielectric constant for such cases can be calculated as [30],

$$\boldsymbol{\varepsilon = \frac{\varepsilon_1 V_1 + \varepsilon_2 V_2 \left[\frac{3\varepsilon_1}{\varepsilon_2 + 2\varepsilon_1}\right]\left[1 + \frac{3V_2(\varepsilon_2 - \varepsilon_1)}{\varepsilon_2 + 2\varepsilon_1}\right]}{V_1 + V_2 \left[\frac{3\varepsilon_1}{\varepsilon_2 + 2\varepsilon_1}\right]\left[1 + \frac{3V_2(\varepsilon_2 - \varepsilon_1)}{\varepsilon_2 + 2\varepsilon_1}\right]}} \qquad \boldsymbol{(4.10)}$$

Using above equation, the dielectric values for HA-10 NKN, HA-20 NKN and HA-30 NKN were calculated to be 30.54, 38.71 and 50.29, respectively.

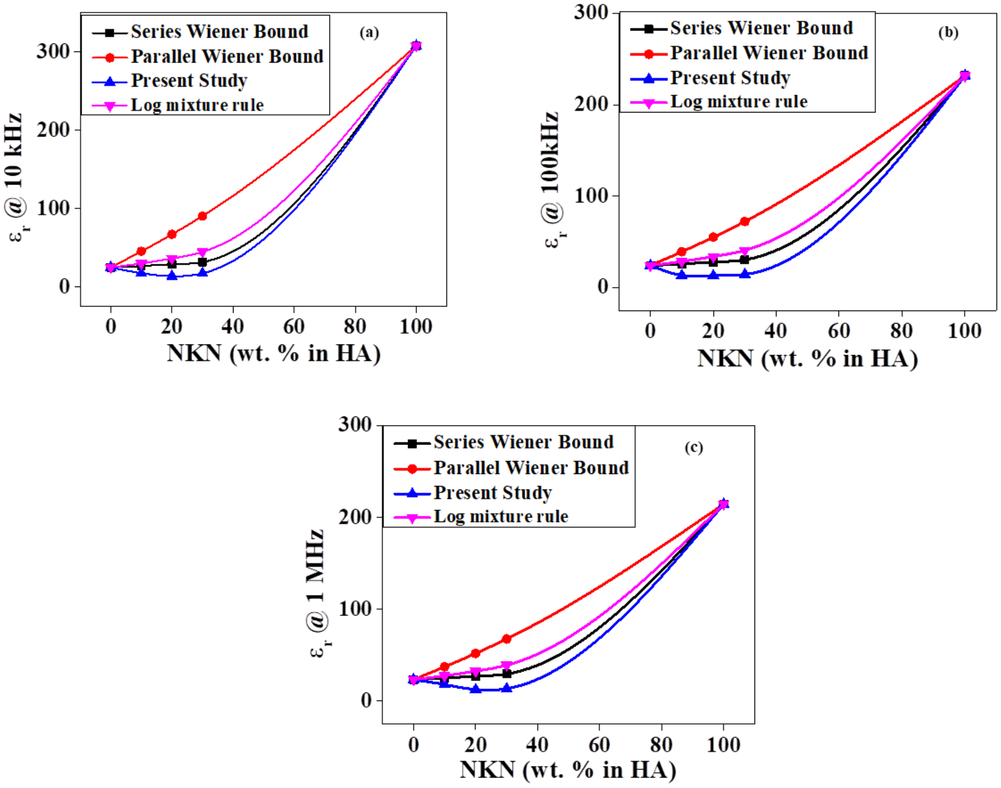

Fig. 4.9. Comparison of dielectric constant between parallel and series Wiener bounds, log mixture rule and present study at frequencies of (a) 10 kHz, (b) 100 kHz and (c) 1 MHz

For polyphase ceramics, the effective dielectric constant can be obtained using the following expression [31],

$$\varepsilon_{eff} = \frac{\varepsilon_m V_m \left[\frac{2}{3} + \frac{\varepsilon_i}{\varepsilon_m}\right] + \varepsilon_i V_i}{V_m \left[\frac{2}{3} + \frac{\varepsilon_i}{\varepsilon_m}\right] + V_i} \qquad (4.11)$$

Where, ε_m, ε_i, V_m and V_i are the dielectric constants and volume fractions of matrix and secondary phase, respectively. Using eq. 4.11, the effective dielectric constant for HA – 10 NKN, HA – 20 NKN and HA – 30 NKN composite were calculated to be 29.81, 35.32 and 42.05, respectively, at 10 kHz of frequency and at room temperature. The values of dielectric constant, calculated using eqs. (10) and (11), are nearly in proximity to each other. Apart from connectivity between constituent phases, microstructure densification, presence of other undetectable phases etc. also play an important role in deciding the effective dielectric constant of the HA – (10 – 30) NKN composite system

4.7 AC conductivity behavior

Figs. 4.10 and 4.11 represent the variation of ac conductivity with temperature at few selected frequencies as well as with frequency at few isothermal temperatures for HA, NKN, HA – 10 NKN, HA – 20 NKN and HA – 30 NKN composites, respectively. The ac conductivity of the sintered samples increases with frequency [Fig. 4.10]. The variation of ac conductivity for HA, NKN and HA – 20 NKN composite is almost similar at higher frequency (~ 1 MHz) [Figs. 4.10 (a), (b) and (d)]. For HA – 10 NKN and HA – 30 NKN composites, ac conductivity decreases initially in lower temperature region (< 300ºC) and increases afterwards, in higher temperature region (> 300ºC) [Figs. 4.10 (c) and (e)].

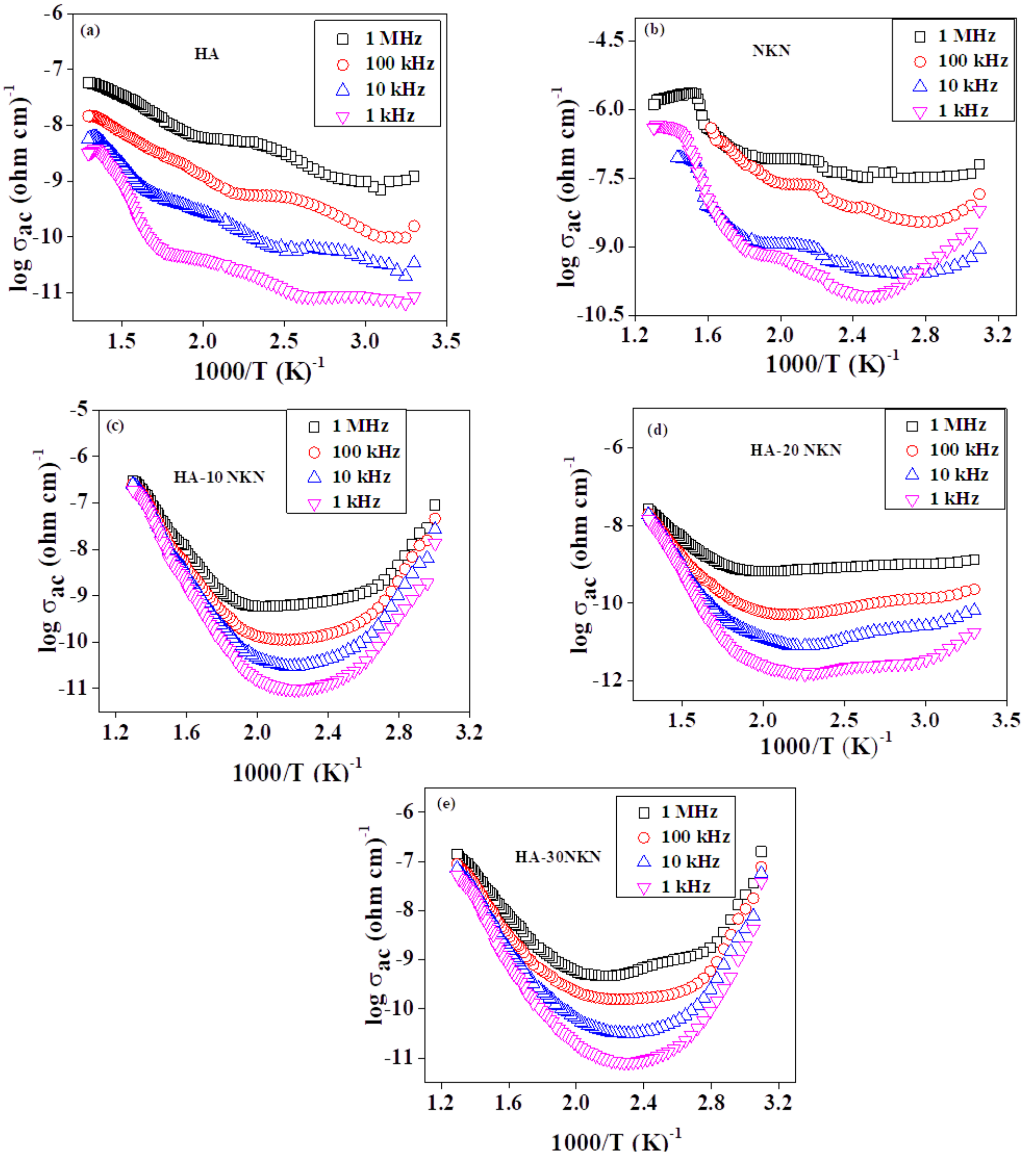

Fig. 4.10. Variation of log σ_{ac} with inverse of temperature at few selected frequencies for (a) HA, (b) NKN, (c) HA – 10 NKN, (d) HA – 20 NKN and (d) HA – 30 NKN composites

The value of ac conductivity of the samples increases marginally at low frequency range [Fig. 4.11]. Monolithic HA and NKN demonstrate almost linear increase in ac conductivity with frequency at low temperature (< 200ºC) [Figs 4.11 (a) and (b)]. At 500ºC, all the developed composites show the almost similar variation in ac conductivity [Figs. 4.11 (c), (d) and (e)].

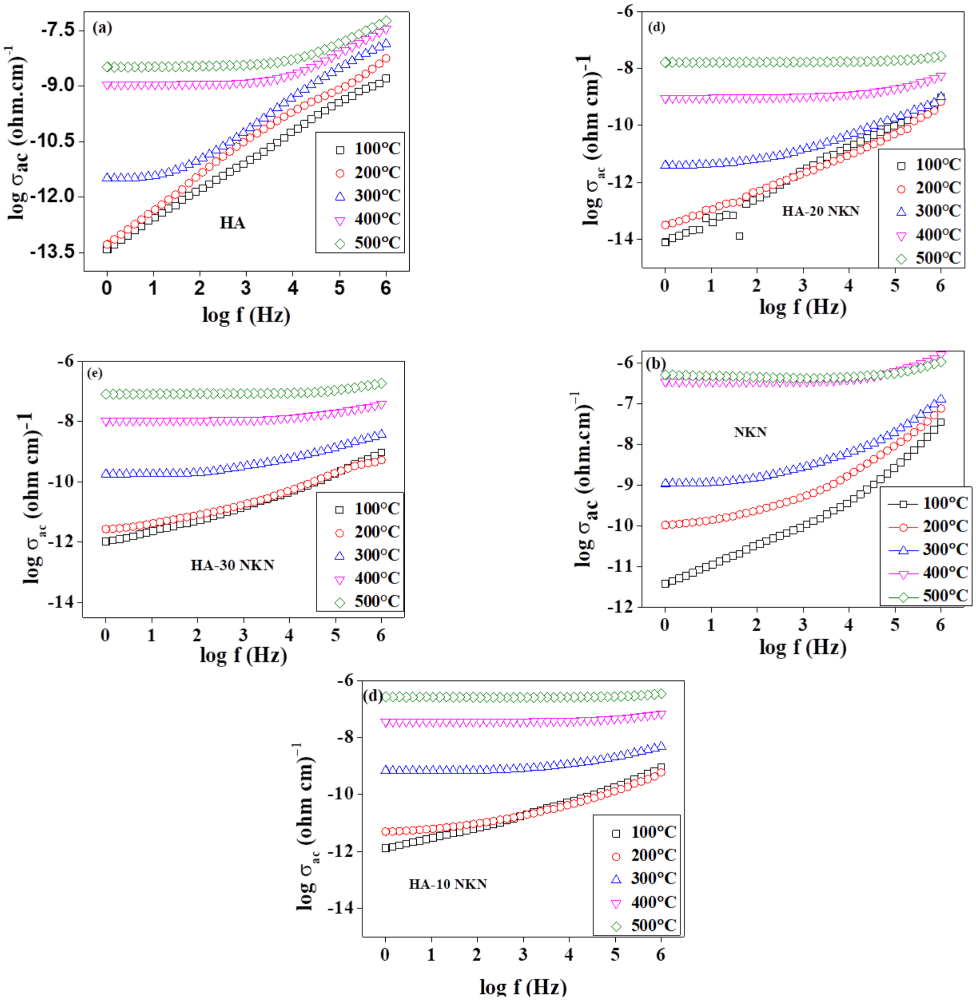

Fig. 4.11 Variation of log σ_{ac} with log f at few selected temperatures for (a) HA, (b) NKN, (c) HA – 10 NKN, (d) HA – 20 NKN and (d) HA – 30 NKN composites

The conduction in HA occurs due to formation of vacancies at the hydroxyl position in the crystal lattice [18]. The conduction mechanism in HA can be described as [32],

$$\mathbf{2\ OH^- + PO_4^{3-} \rightarrow O^{2-} + HPO_4^{3-} + OH \rightarrow O^{2-} + PO_4^{3-}HOH + \square OH^-} \qquad \mathbf{(4.12)}$$

Where, □ denotes the vacancy.

The increase in conductivity at high temperature is due to hopping of H^+ ions to O^{2-} sites as [33],

$$\mathrm{Ca_{10}(PO_4)_6(OH)_2} \rightarrow \mathrm{Ca_{10}(PO_4)_6(O\,H)_{2-2x}\,O_x\square_x} + \mathrm{xH_2O} \qquad (4.13)$$

At lower temperature, HA surface absorbs water due to its hygroscopic nature. The transfer of proton (H^+) in absorbed water can be one of the possible reasons for conduction in HA at room temperature [34]. Eqs. 4.2 – 4.5 represent the formation of defects during high temperature treatment, which affect the conductivity of sintered NKN. In present study, room temperature ac conductivity for the fabricated composites i.e., HA – 10 NKN, HA – 20 NKN and HA – 30 NKN composites were measured to be 2.69×10^{-8}, 6.84×10^{-11} and 5.76×10^{-8} $(\text{ohm cm})^{-1}$ respectively, at 10 kHz of frequency.

4.8 Impedance analysis

Figs. 4.12 (a-e) represent the complex impedance plots (Nyquist plots) for HA, NKN and [HA – (10 – 30) NKN] composites at temperatures of 100˚C, 200˚C, 300˚C, 400˚C and 500˚C, respectively [35]. Fig 4.12 demonstrates that the center of semicircular arcs lies below the real Z' axis which is indicative of multiple relaxation processes in the sintered samples [36]. The displacement of the peaks toward origin with increase in temperature is due to reduction in overall resistivity of the samples [Figs 4.12 (a) - (e)].

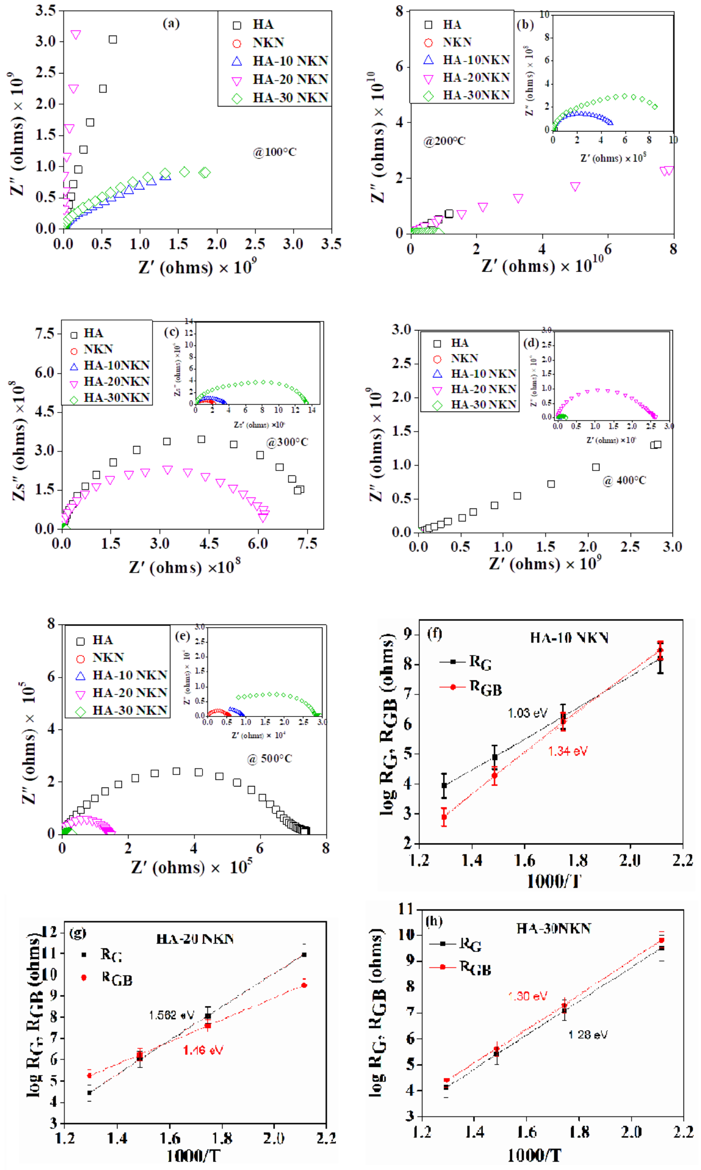

Fig. 4.12. Complex plane impedance plots for HA, NKN, HA-10 NKN, HA- 20 NKN and HA-30 NKN composites at temperatures (a) 100˚C, (b) 200˚C, (c) 300˚C, (d) 400˚C, (e) 500ºC; (f), (g) and (h) represent the variation of log (R_g, R_{gb}) vs 1000/T

The complex impedance plot reveals the behavior of grains and grain boundaries in terms of resistances and capacitances. The grain effect is associated with high frequency semicircle, whereas medium frequency semicircle is related to the grain boundary effect and low frequency semicircle represents the electrode interface effect [37].

Complex modulus (M*) can be obtained by using[36] the expressions $M' = \omega\, CoZ''$ and $M'' = \omega\, Co\, Z'$ where, ω = 2лf (angular frequency), C_o is open cell capacitance and Z′, Z″, M′, M″ are the real and imaginary components of impedance and modulus, respectively. For the composites, resistances of grains and grain boundaries at temperatures of 200ºC, 300ºC, 400ºC and 500ºC have been plotted with inverse of temperature. With the help of linear fit in plot, log (R_g, R_{gb}) vs 1000/T [Figs. 4.12 (f-h)], activation energies of grain (E_g) and grain boundary (E_{gb}) for HA – 10 NKN composite are calculated to be 1.03 and 1.34 eV, respectively. However, E_g and E_{gb} values for HA – 20 NKN and HA – 30 NKN composites are 1.46 and 1.56 eV as well as 1.28 and 1.30 eV, respectively.

Figs. 4.13 (a - e) represent the impedance and modulus spectroscopic behavior for pure HA, NKN, HA-10 NKN, HA-20 NKN and HA-30 NKN composites, respectively. The variation of complex impedance (Z″) and complex modulus (M″) with frequency provide the spectrum of conduction mechanisms [38]. As the frequency increases, the Z″ value decreases for a given temperature in the lower frequency region. At higher temperature (> 200˚C), impedance values are independent with the frequency variation (up to 1 MHz) [Fig. 4.13]. As frequency increases, the relaxation peaks in modulus spectroscopic plots are shifted towards to higher temperature region, satisfying the equation, ω.τ = 1. The variation of peaks with respect to the position and amplitude in frequency scale is occurring due to space charge and dipolar polarization mechanisms8 [Figs. 4.11 (a – e)].

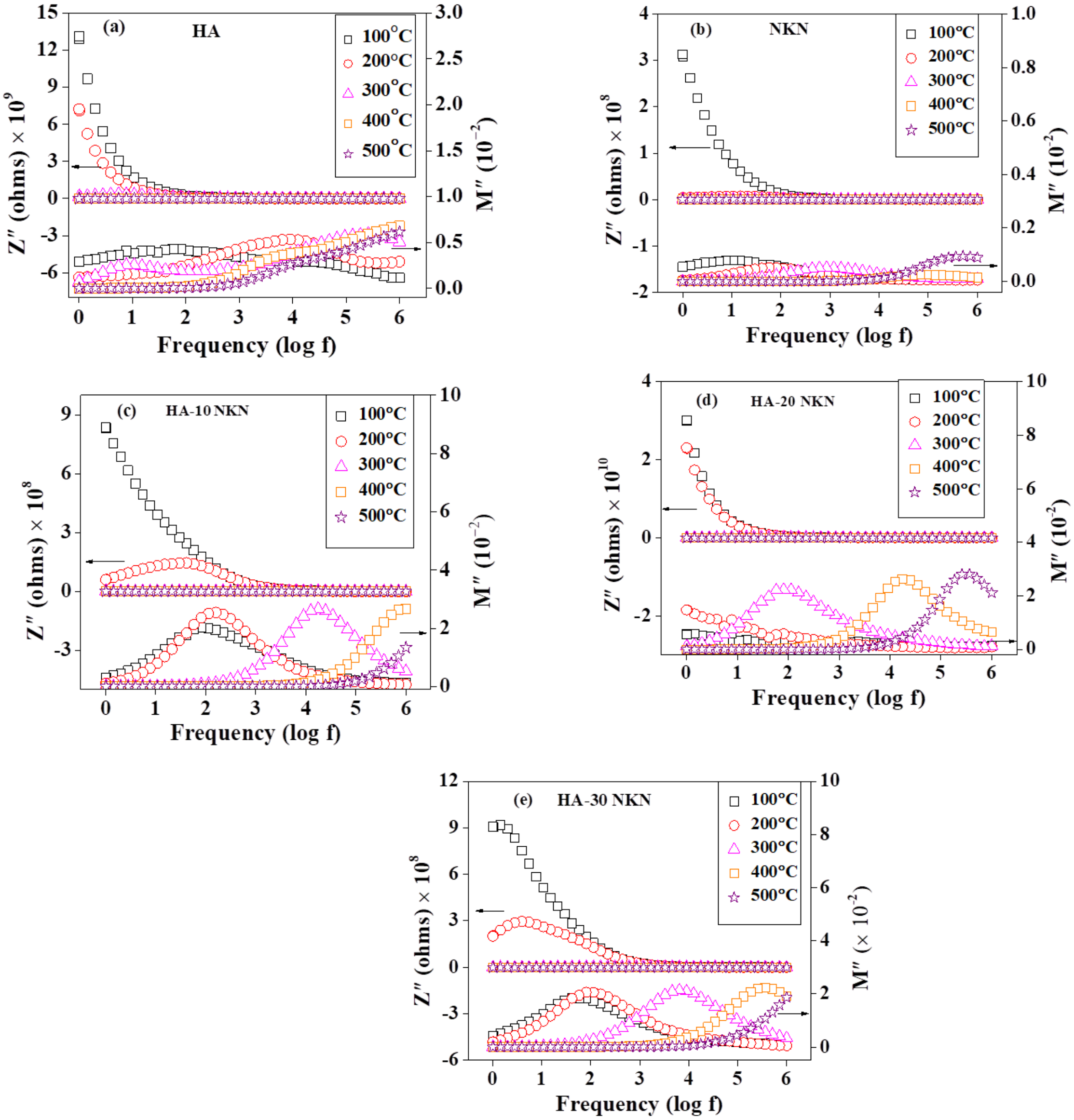

Fig. 4.13. Impedance and modulus spectroscopic plots for (a) HA, (b) NKN, (c) HA-10 NKN, (d) HA-20 NKN and (e) HA-30 NKN composites

Oxygen vacancies and other defects are created due to high sintering temperature for HA and NKN [25]. Owing to the oxygen vacancies, the movement of space charge increases with increase in temperature which can be suggested as one of the possible reasons for shifting of peaks toward the higher frequencies on frequency scale [39]. The present study reveals that the addition of piezoelectric secondary phase improves electrical and dielectric properties of

HA. Overall, the dielectric constant as well as ac conductivity of the optimally processed composite samples is comparable to that of the human bone.

4.9 Antibacterial response

4.9.1 MTT assay

Figs. 4.14 (a) and (b) represent the variation in mean optical densities of gram positive (*S. aureus*) and gram negative (*E. coli*) bacterial cells on unpolarized and polarized monolithic HA (control) and HA - (10 - 30) NKN composite samples. The incorporation of piezoelectric NKN secondary phase decreases the bacterial adhesion on HA. It is clearly seen by statistical analyses that the unpolarized and polarized HA – (10 – 30) NKN exhibited significant difference in mean optical density than monolithic HA. Figs. 4.14 (a) and (b) suggested that the unpolarized, negatively and positively polarized HA - (10 - 30) NKN composites exhibited the statistically significant reduction in the viability for both the bacterial cells i.e., *S. aureus* and *E. coli* with respect to the uncharged HA [represented as * in Figs. 4.14 (a) and (b)].

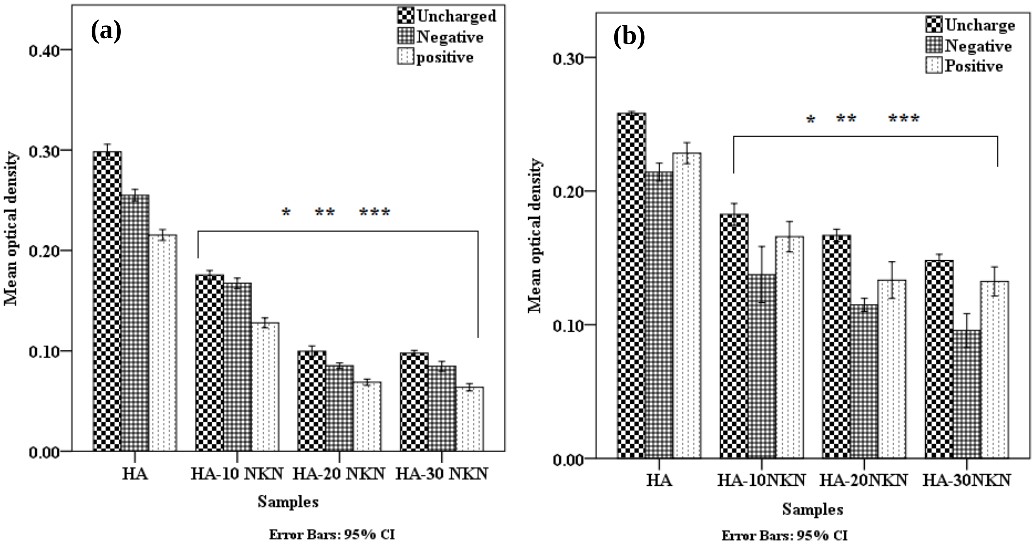

Fig. 4.14. Polarization induced antibacterial response of HA, HA-10 NKN, HA-20 NKN and HA-30 NKN composites for (a) gram positive (S. aureus) and (b) gram negative (E. coli) bacteria. Asterisk (*), (**) and (***) mark represent the significant difference in optical density of the bacterial cells for the uncharged, negatively and positively charged samples at $p < 0.05$*, with respect to the monolithic HA.*

Irrespective of incorporation of NKN secondary phase in HA, statistically significant reduction in mean optical density of *S. aureus* and *E. coli* bacterial cells has been observed on negatively and positively charged HA - (10 - 30) NKN composite samples, respectively, with respect to that of negatively and positively charged HA [represented as ** and ***, respectively, in Figs. 4.12 (a) and (b)]. The viability of *S. aureus* and *E. coli* bacterial cells have been reduced to about 22 % and 37 % on the positively and negatively charged surfaces of HA - 30 NKN composite samples, respectively, with respect to uncharged monolithic HA.

4.9.2 Live / dead assay

Figs. 4.15 and 4.16 demonstrate the live and dead bacterial cells, adhered on unpolarized and polarized monolithic HA and HA - (10 - 30) NKN composite samples. It can be clearly observed that the addition of piezoelectric NKN secondary phase in HA reduces the population of live cells (green) with respect to monolithic HA. Figs. 4.15 and 4.16 illustrate that the positively and negatively charged HA - 30 NKN composites exhibit more population of dead bacterial cells for both, *S. aureus* and *E. coli* bacteria. Overall, the qualitative analyses corroborate the quantitative analyses for unpolarized and polarized HA - (10 - 30) NKN composite samples.

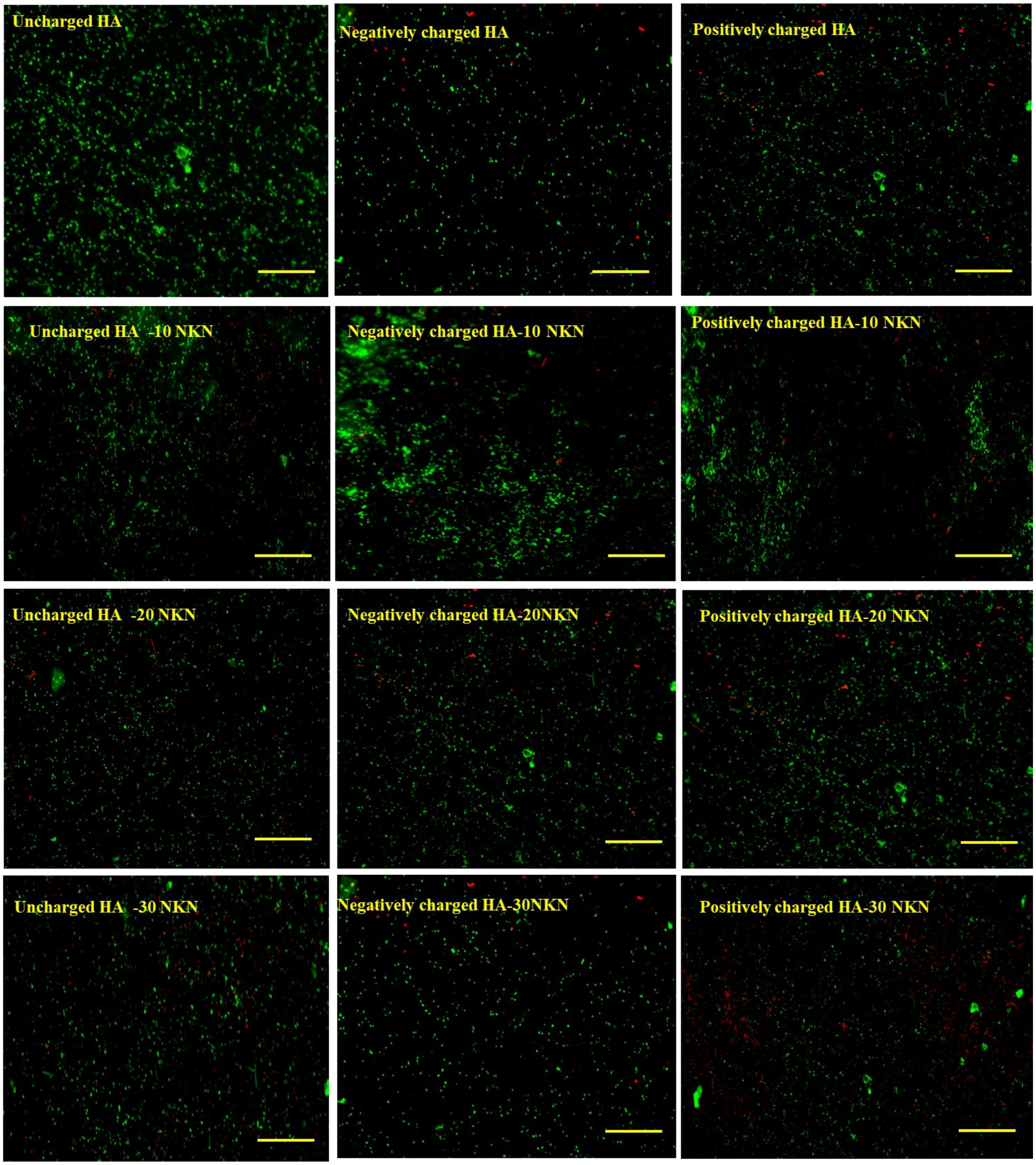

Fig. 4.15. Fluorescence microscopy images of live (green) and dead (red) S. aureus bacterial cells, cultured on unpolarized, positively and negatively polarized HA and HA-(10-30) NKN composite samples. Scale bar corresponds to 100 µm.

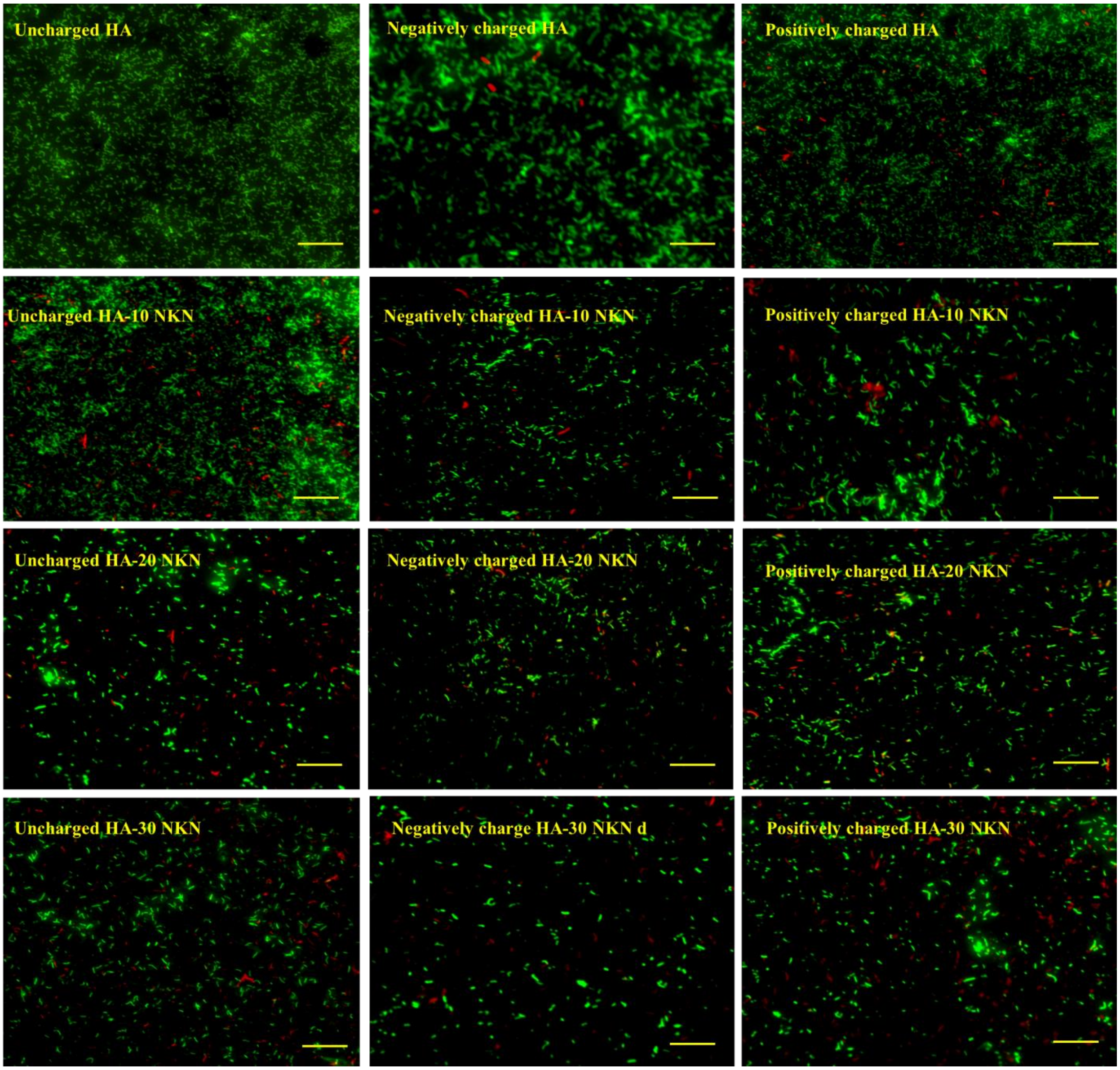

Fig. 4.16. Fluorescence microscopy images of live (green) and dead (red) E. coli bacterial cells, cultured on unpolarized, positively and negatively polarized HA and HA - (10 – 30) NKN composite samples. Scale bar corresponds to 100 µm.

4.9.3 Super oxide radical (SOD) assay

SOD is an antioxidant enzyme that catalyses the dismutation of superoxide radical into H_2O_2 and O_2 [40]. In general, SOD assay comprises of two systems: SOD generating and SOD detecting systems. Here, quantification of superoxides (O_2^-) was done as a measure of SOD assay. In this assay the cultured samples were incubated for 8 h. After incubation lysozyme (1 mg/ml) was added and incubated further for 1 h. Then centrifugation was done at 10000 rpm and 4ºC temperatures for 10 min, and the supernatant was collected for further analyses. The supernatant (0.5 ml) was taken in a test tube and other regents, 0.01 M PBS (pH 7.8), 130 mM methionine, 60 μM riboflavin, 0.5 mM EDTA and 0.75 mM NBT were added in the test tube. The final solution was kept in front of fluorescent light for 6 min and absorbance was taken at 560 nm, which is directly proportional to the produced O_2^- ions [41].

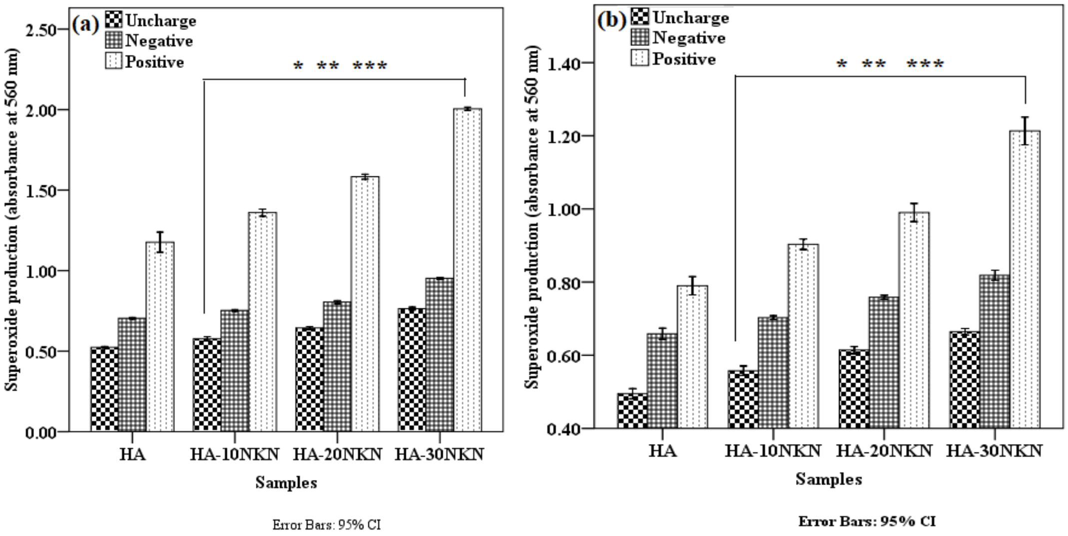

Fig. 4.17. Superoxide production (ROS generation) on unpolarized and polarized HA, HA-10 NKN, HA-20 NKN and HA-30 NKN composites for (a) gram positive (S. aureus) and (b) gram negative (E. coli) bacteria. Asterisk (*), (**) and (***) marks represent the significant difference in superoxide production by the bacterial cells for the uncharged, negatively and positively charged samples at $p < 0.05$, with respect to the uncharged, negatively and positively monolithic HA.

Figs. 4.17 (a) and (b) represent the superoxide production in vicinity of polarized and unpolarized HA, HA – 10 NKN, HA – 20 NKN and HA – 30 NKN composites samples, cultured with *S. aureus* and *E. coli*, respectively. The statistical significant difference in superoxide production by the *S. aureus* and *E. coli* bacterial cells for unpolarized and polarized HA – 10 NKN, HA – 20 NKN and HA – 30 NKN composites has been observed with respect to unpolarized monolithic HA [represented as * in Figs. 4.17 (a) and (b)]. Also, the significant difference has been observed in superoxide production by *S. aureus* and *E. coli* bacterial cells on negatively and positively charged HA - (10 - 30) NKN composite samples, respectively, with respect to that of negatively and positively charged HA [represented as ** and ***, respectively, in Figs. 4.17 (a) and (b)]. The statistical significant different in production of superoxide on positively polarized samples has been obtained in comparison to negatively polarized and unpolarized samples, irrespective of sample and bacterial type. However, also the addition of NKN secondary phase in HA also revealed the significance difference in superoxide production.

4.9.4 Catalase Assay

Catalase assay was used to determine the activity of enzyme catalase in terms of hydrogen peroxide (H_2O_2) dissociation, which is measured spectrophotomatrically at 240 nm. Briefly, 0.1 ml of centrifuged bacterial culture (containing enzyme) was mixed with phosphate buffer (1.9 ml of pH 7.0). Following this, 30 mM H_2O_2 (substrate) was added and the absorbance was taken spectrophotometrically at 240 nm. The dissociation of H_2O_2 by *E. coli* and *S. aureus* bacterial cells, cultured on polarized and unpolarized HA and HA NKN composite surfaces were calculated in terms of catalase activity/sec [42],

$$\text{Catalase activity (K)} = \frac{2.3}{\Delta t} \times \log \frac{E_1}{E_2}$$

Where, E_1 and E_2 represent the absorbance, at t = 0 and t = 30 sec, respectively.

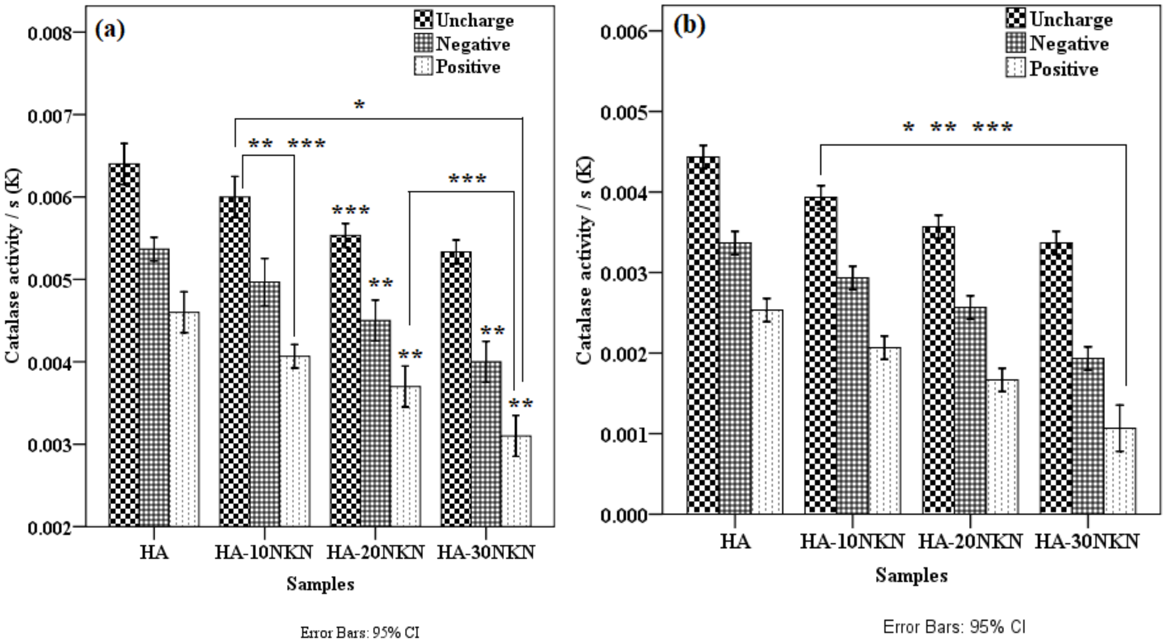

Fig.4.18. The catalase activity/ sec. of (a) S.aureus and (b) E. coli bacteria, cultured on unpolarized and polarized HA, HA – 10 NKN, HA – 20 NKN and HA – 30 NKN composites. Asterisk (*) mark represents the significant difference among all composite samples with respect to unpolarized HA at $p < 0.05$. Asterisk marks (**) and (***) represents the significant difference among all composite samples with respect to negatively polarized and positively polarized HA, respectively, at $p < 0.05$.

Figs. 4.18 (a) and (b) represent the catalase activity in vicinity of polarized and unpolarized HA, HA – 10 NKN, HA – 20 NKN and HA – 30 NKN composites samples, cultured with *S. aureus* and *E. coli* bacteria, respectively. The statistical significant difference in catalase activity of the *S. aureus* and *E. coli* bacterial cells is observed for unpolarized and polarized HA – 10 NKN, HA – 20 NKN and HA – 30 NKN composites with respect to unpolarized and polarized monolithic HA [represented as *, ** and *** in Figs. 4.18 (a) and (b)]. In comparison to positively charged HA, the unpolarized and polarized composite samples exhibited significant difference in catalase activity of *S. aureus* except negatively polarized HA – 20 NKN composite [represented as *** in Fig. 4.18 (a)]. Catalase activity of *E. coli* bacterial cells for unpolarized and polarized composites reveal the significant difference with respect to the positively polarized HA [represented as *** in Fig. 4.18 (b)].

Catalase is an antioxidant enzyme that decomposes hydrogen peroxide into water and oxygen, which protect the cells from oxidative damage [43–45]. Here, the catalase activity is evaluated in terms of H_2O_2 decomposition. The absorbance value represents the amount of H_2O_2 remained in reaction mixture. Therefore, the absorbance value is inversely proportional to the catalase activity. As can be seen in Fig. 4.18, the reduced catalase activity means higher H_2O_2 which leads to oxidative damage of bacterial cells. Statistical analyses reveal that catalase activity was reduced on positively polarized surface in comparison to negatively polarized and unpolarized surfaces, irrespective of sample and bacterial types, which in concluded as higher H_2O_2 in vicinity of positively polarized surface. Also, the H_2O_2 production is appeared to be increased with increasing proportion of NKN secondary phase.

4.9.5 Lipid peroxidation (LPO) assay

LPO assay was used to evaluate level of oxidative stress, in terms of end product of lipid peroxidation reaction, i.e.; malondialdehyde (MDA) and 4-hydroxynonenal (4 HNE). Here, lipid peroxidation is assessed in terms of MDA which is measured spectrophotometrically at 532 nm. The produced aldehydes are toxic in nature which damages the DNA and protein of bacterial cells. Briefly, 500 µL of centrifuged culture supernatant (as mentioned in section 4.8.3) was mixed with 500 µL tris HCl in a test tube and incubated for 2 h at 37 ºC, followed by addition of 1000 µL trichloroacetic acid (TCA). This reaction mixture was centrifuged for 10 min at 3500 rpm. After that, 1.5 ml of thiobarbituric acid (TBA) was added to equal volume of centrifuged solution and boiled for 10 min at 100ºC. Following this, 1 ml of distilled water (D.W.) was added and absorbance were taken at 532 nm. The LPO activity was calculated using the formula [46],

$$\mathrm{MDA/mg\ protein} = \frac{\mathrm{OD\ 532} \times \mathrm{reaction\ Volume} \times 10^{9}}{\mathrm{Sample\ volume} \times 1000 \times \mathrm{Extinsion\ coefficientof\ MDA}}$$

Extinsion coefficient of MDA has been taken to be $1.56 \times 10^{5}\mathrm{M}^{-1}\mathrm{cm}^{-1}$ [47,48].

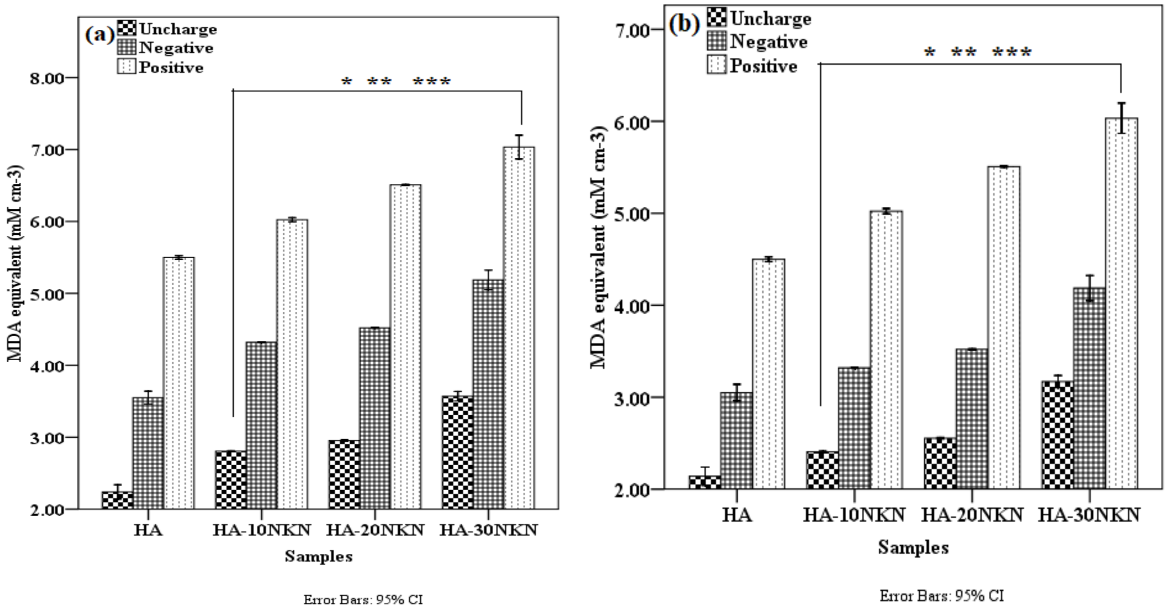

Fig.4.19. Lipid peroxidation in terms of MDA equivalent for (a) S.aureus and (b) E. coli bacteria, cultured on polarized and unpolarized HA, HA-10 NKN, HA-20 NKN and HA-30 NKN composites. Asterisk (*) mark represents the significant difference among all the composite samples with respect to unpolarized HA at $p < 0.05$. Asterisk marks (**) and (***) represent the significant difference among all composite samples with respect to negatively and positively polarized HA, respectively, at $p < 0.05$.

Figs. 4.19 (a) and (b) represent the calculated MDA equivalent for *S. aureus* and *E. coli* bacteria, cultured on unpolarized and polarized HA, HA – 10 NKN, HA – 20 NKN and HA –

30 NKN composite samples, respectively. It can be clearly seen that there is statistical significant difference in MDA equivalent for the *S. aureus* and *E. coli* bacterial cells for unpolarized and polarized HA – 10 NKN, HA – 20 NKN and HA – 30 NKN composites with respect to unpolarized monolithic HA [represented as * in Figs. 4.19 (a) and (b)]. Irrespective of incorporation of NKN secondary phase in HA, statistically significant difference in MDA equivalent for *S. aureus* and *E. coli* bacterial cells has been observed on negatively and positively charged HA - (10 - 30) NKN composite samples, respectively, with respect to that of negatively and positively charged HA [represented as ** and ***, respectively, in Figs. 4.19 (a) and (b)]. Lipid peroxidation is a well-established mechanism of oxidative damage of polyunsaturated lipids. Under oxidative stress, the polyunsaturated fatty acid decompose to form malondialdehyde (MDA), which is measured as an indicator of lipid peroxidation [49-51] MDA forms an adduct with thiobarbituric acid (TBA) which gives maximum absorbance at 532 nm [50]. Higher absorbance resembles more MDA formation, which ultimately depicts the more lipid peroxidation resulting in more cell death. Fig 4.19 shows the amount of MDA appears to increase with increased proportion of NKN secondary phase irrespective of bacteria type. Therefore, the antibacterial nature of NKN can be realized. Also, the level of MDA on positively polarized sample surface is higher in comparison to negative and unpolarized samples, irrespective of sample and bacterial types.

4.9.6 Protein estimation assay

In this assay, first of all reagent A (consisting of 0.1 NaOH and 2 % Na_2CO_3) and reagent B (comprises of 0.5 % $CuSO_4$ and 1.35 % potassium sodium tartrate) were mixed in specified proportion of (48 % of regent A and 2 % of regent B) to make reagent C. After that, 20 µl supernatant of centrifuged culture was mixed with 980 µl of distilled water. Following this, 5 ml of reagent C was added to this solution and incubated for 10 min at room temperature. Thereafter, 500 µl of follins regent was added and incubated further for 30 min that change the colour of solution to blue which is measured spectrophotometrically, at 750 nm. The protein concentration was calculated according to Lowry method using bovine serum albumin (BSA) as standard [52].

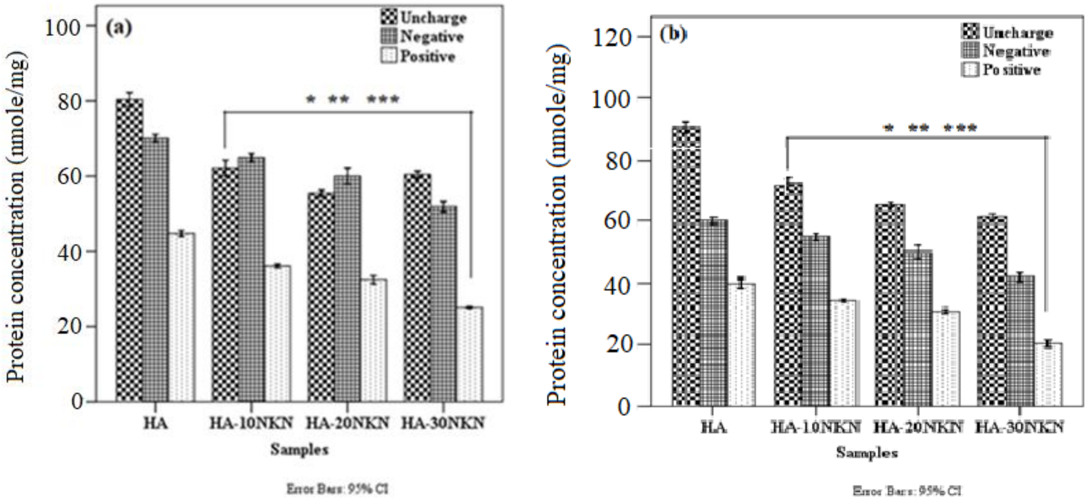

Fig. 4.20 The concentration of protein for (a) S. aureus and (b) E. coli bacteria cultured on polarized and unpolarized HA, HA – 10 NKN, HA – 20 NKN and HA – 30 NKN composites. Asterisk (*) mark represents the significant difference among all the composite samples with respect to unpolarized HA at $p < 0.05$. Asterisk marks (**) and (***) represent the significant difference among all composite samples with respect to negatively and positively polarized HA, respectively, at $p < 0.05$.

The basic principle of the present methodology is that, the proteins react with alkaline cupric sulfate to form a tetradentate cuprous complex in the presence of sodium potassium tartrate [53]. This Cu^+, present in cuprous complex, then reduces the Follin reagent to deep blue color solution, which is monitored spectrophotometrically at 750 nm [53]

Protien + Cu^{2+} $\xrightarrow{\quad}$ tetradentate cuprous complex $\xrightarrow{\quad}$ reduced follin reagent

Figs. 4.20 (a) and (b) represent the protein estimation in *S. aureus* and *E. coli* bacteria, cultured on unpolarized and polarized HA, HA – 10 NKN, HA – 20 NKN and HA – 30 NKN composite samples, respectively. The statistical significant difference in protein content for the *S. aureus* and *E. coli* bacterial cells have been observed for unpolarized and polarized HA – 10 NKN, HA – 20 NKN and HA – 30 NKN composites with respect to unpolarized monolithic HA [represented as * in Figs. 4.20 (a) and (b)]. Irrespective of incorporation of NKN secondary phase in HA, statistically significant difference in protein content for *S. aureus* and *E. coli* bacterial cells has been observed on negatively and positively charged HA - (10 - 30) NKN composite samples, respectively, with respect to that of negatively and positively charged HA [represented as ** and ***, respectively, in Figs. 4.20 (a) and (b)]. Figs 4.20 (a) and (b) reveal that the total protein content was decreases significantly on positively polarized surface in comparison to negatively polarized and unpolarized surfaces, irrespective of sample and bacterial types. Also, the amount of protein is observed to reduce with increasing proportion of NKN secondary phase.

Both, the bacterial cells consist of the layer of lipopolysaccharides and peptidoglycan which possess negative charge [54,55]. It has been suggested that bacterial cells get repelled by negatively charged surface whereas the positively charged surfaces depolarized the membrane of the cells which leads to the damage of bacterial cells [55,56]. It has been reported that antibacterial behavior of the samples can be influenced by the hydrophilicity of the surfaces [57]. Polarization enhances the hydrophilic nature of the sample surfaces. It has been suggested that the generation of reactive oxygen species (ROS) such as hydroxyl ions, peroxides, superoxides etc. on the substrates is another factor which affects the antibacterial response due to their toxic nature towards bacterial cells [58,59]. Overall, antibacterial mechanism is shown in fig. 4.21

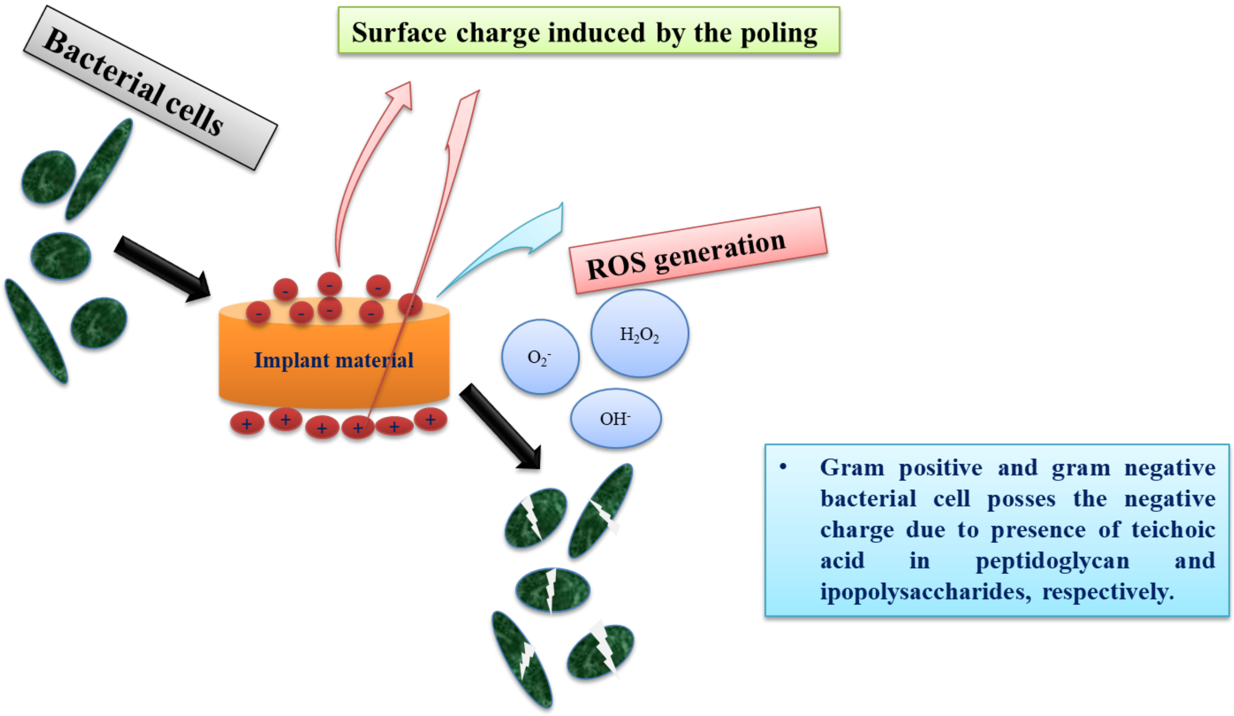

- Gram positive and gram negative bacterial cell posses the negative charge due to presence of teichoic acid in peptidoglycan and ipopolysaccharides, respectively.

Fig. 4.21 Schematic representing the antibacterial activity due to the ROS generation

4.10 *In vitro* cytocomapatibity

4.10.1 Cell Viability

Fig. 4.22 represents the MTT assay results for untreated and electric field (E-field) treated MG-63 cells, cultured on, unpolarized and polarized HA and HA-30 NKN, after 3, 5, and 7 days of incubation in terms of mean OD. The statistically significant difference in cell proliferation is observed for the cells, cultured for 5 and 7 days in comparison to cells, incubated for 3 days, irrespective of sample type and E-field treatment. It has also been observed that negatively polarized surface promote cell proliferation in contrast to positively polarized and unpolarized surfaces. Also within same incubation period, it has been found that cell proliferation rate is higher for HA - 30 NKN in comparison to pure HA and control.

Further, the proliferation is observed to increase for E - field treated negatively polarized surfaces. It can, therefore, be suggested that surface charge in combination with external E-field, synergistically promote cell growth and proliferation.

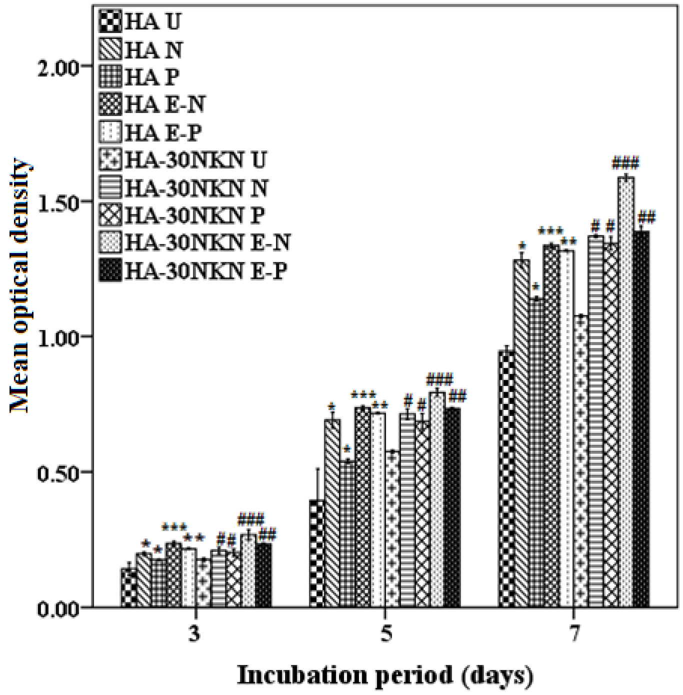

Fig.4.22. Combined effect of surface polarization and electric field treatment on in vitro cytocompatibility of HA and HA – 30 NKN composites using MG-63 cells. ***(*)*** *and* ***(#)*** *represent the significant difference in optical density between uncharged HA and HA – 30 NKN. (**) and (##) show the statistically significant difference in optical density for electric field treated positively polarized HA and HA – 30 NKN composite with respect to positively polarized HA and HA – 30 NKN composite and (***) and (###) show statistically significant difference in optical density for electric field treated negatively polarized HA and HA – 30 NKN with respect to negatively polarized HA and HA – 30 NKN composite.*

It has been demonstrated by several researchers that polarization induced surface charge can enhance osteoblast cell proliferation and new bone formation [60 –65]. It has also been reported that the negatively polarized HA surfaces promote osteobonding ability in comparison to positively polarized surfaces [66 - 68]. This is due to the fact that the cations like Ca^{2+} ions, present in media are attracted towards negatively charged HA and promote the attachment of cell adhesion factors (integrin and fibronectin protein), which accelerate the cell adhesion [69]. Thus, the electrostatic interaction of ions Ca^{2+}, PO_4^{3-} etc. with charged surface is one of the possible factors that facilitate cell adhesion and proliferation in the vicinity of charged surfaces. In addition, external electrical stimulation further accelerates cell growth and proliferation, and which results in increased cell density [70,57]. A number of studies revealed that the electrical stimulation open the voltage gated Ca^{2+} channels which promote the intracellular Ca^{2+} influx that enhances the cell proliferation [71-73] The influx of Ca^{2+} activates Akt signaling pathway, that further promotes cell proliferation [74].

4.10.2 Morphological study

Fig. 4.23 demonstrates the fluorescence images of untreated and electric field (E-field) treated MG-63 cells, cultured on unpolarized and polarized HA and HA - 30 NKN samples. It is clearly observed that, the cell density is higher on electric field treated surface in comparison to untreated samples. Also, the cells are appeared to be more flattened which suggest better cell functionality. It has also been observed that cell density is higher on negatively polarized surface in comparison to positively polarized and unpolarized surfaces. In addition, cell density is higher and the cells are better spreaded over the HA – 30 NKN composite sample in comparison to pure HA surface, irrespective of surface charge and electrical stimulation. It has been reported that, in addition to cell proliferation, polarized material surface also promotes early cell adhesion and spreading [75]. It can, therefore, be suggested that the incorporation of piezoelectric NKN secondary phase as well as the combined action of surface polarization and external electric field treatment enhances the biocompatibility of composite samples.

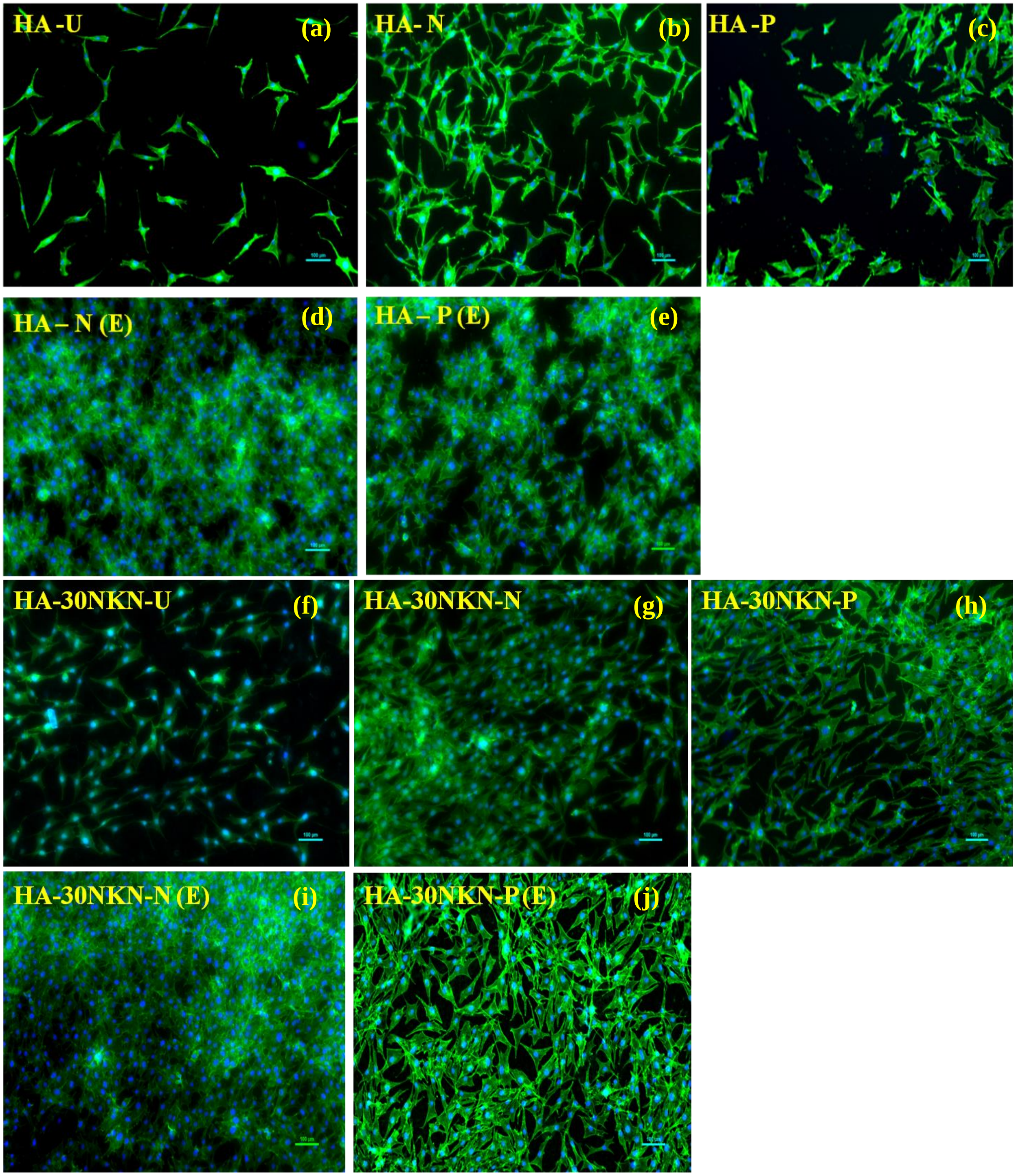

Fig.4.23. Fluorescence images, demonstrating the morphology of osteogenic MG63 cells, while cultured for 72 h on (a) uncharged HA, (b) negatively polarized HA, (c) positively polarized HA, (d) E-field treated negatively polarized HA, (e) E-field treated positively polarized HA (f) uncharged HA – 30 NKN composite, (g) negatively polarized HA – 30 NKN composite, (h) positively polarized HA – 30 NKN composite, (i) E-field treated negatively polarized HA – 30 NKN composite and (j) E-field treated positively polarized HA – 30 NKN composite. The E-field strength was 1 V/cm. The scale bars correspond to 100 μm.

Overall, the incorporation of piezoelectric NKN in HA improves the mechanical, electrical, polarization induced antibacterial behavior and biocompatibility of HA.

4.11 Closure

This chapter demonstrates that dielectric and electrical response of HA can be enhanced by the incorporation of biocompatible piezoelectric NKN secondary phase to achieve bone like electrical properties. HA – x NKN (x = 0, 10, 20, 30, 100 wt %) ceramic composites were optimally processed by solid state synthesis with reasonably good densification, achieved by cold isostatic pressing. The optimal processing parameters facilitate the presence of phase pure HA and NKN in the developed composite system without any reaction or dissociation between these constituent phases. The addition of NKN in HA significantly enhances the mechanical properties. Among the developed composite samples, HA - 30 NKN exhibits the maximum hardness, fracture toughness, compressive and flexural strength due to additional toughening, provided by the incorporation of piezoelectric NKN. The variations in dielectric constant and loss are associated with the interfacial or space charge polarization due to presence of the phases with different conductivities. Nyquist plots reveal the conduction mechanism in such composite system, where ionic conduction due to hydroxyl ions and oxygen vacancies are observed to be the dominant conduction mechanisms. The antibacterial behavior of HA has been augmented by the incorporation of piezoelectric NKN secondary phase in HA against gram positive (*S. aureus*) and gram negative (*E. coli*) bacterial cells. Statistical analyses revealed that the viability of gram positive (*S. aureus*) and gram negative (*E. coli*) bacterial cells reduces significantly on positively and negatively charged surfaces of HA - NKN composite. In addition, the quantitative and qualitative analyses reveal the enhanced cytocompatibility of HA and HA-NKN composite due to combined action of surface polarization and electrical stimulation. In summary, the inclusion of piezoelectric NKN secondary phase in HA has been observed to improve the mechanical, polarization induced antibacterial behavior and *in vitro* biocompatibility of HA. Overall, HA- x NKN system can be suggested as the potential candidate for electro-active orthopedic implant applications.

References

---

1. M.H. Fathia, A. Hanifia, V. Mortazavi, **“**Preparation and bioactivity evaluation of bone-like hydroxyapatite nanopowder**,”** *Journal of Materials Processing Technology***., 202** (2008)536–542**.**

2. E. Mohseni, E. Zalnezhad, A.R. Bushroa, “Comparative investigation on theadhesion of hydroxyapatite coating on Ti-6Al-4V implant: a review paper,” *International Journal of Adhesion and Adhesives.,* **48** (2014) 238-257.

3. M. Jarcho, “Calcium phosphate ceramics as hard tissue prosthetics,” *Clinical Orthopaedics and Related Research***157**(1981)259–278.

4. L. L. Hench, “Bioceramics,” *Journal of the American Ceramic Society,* **81 (7)** (1998) 1705-1728.

5. I. Sopyan, M. Mel, S. Ramesh, K.A. Khalid, “Porous hydroxyapatite for artificial bone applications,” *Science and Technology of Advanced Materials.,* **8** (2007)116–23.

6. K.Y. Lee, M. Park, H.M. Kim, Y.J. Lim, H.J. Chun, H. Kim, “Ceramic bioactivity: progresses, challenges and perspectives,” *Ann. Biomed. Mater.,* **1** (2006), 31–38.

7. K.A. Hing, S.M. Best, K.E. Tanner, W. Bonfield, P.A. Revell, “Mediation of bone ingrowth in porous hydroxyapatite bone graft substitutes,”. *Journal of Biomedical Materials Research.* A, **68** (2003), 187–200.

8. A. K. Dubey, B. Basu, K. Balani, Guo R., A. S. Bhalla, “Dielectric and Pyroelectric Properties of HAp-BaTiO3 Composites,” *Ferroelectrics,* 423 (2011), 63–76.

9. H. Gheisari, E. Karamian, M. Abdellahi, “A novel hydroxyapatite –Hardystonitenano composite ceramic,” Ceramic International., **41(4)** (2015), 5967-5975.

---

10. D.Q. Zhang, Z.C. Qin, X.Y. Yang, H.B. Zhu, M.S. Cao, “Study on synthesis and evolution of sodium potassium niobateceramic powders by an oxalic acid-based sol–gel method,” *Journal of Sol-Gel Science and Technology.*, **57**(2011)31–35.

11 P. K. Zysset, X. E. Guo, C. E. Hoffler, K. E. Moore, S. A. Goldstein, “Elastic modulus and hardness of cortical and trabecular bone lamellae measured by nano indentation in the human femur,” *Journal of Biomechanics* **32** (1999) 1005-1012.

12. X.M. Chen, B. Yang, A new approach for toughening of ceramics, *Materials Letters* **33** (1997) 37–240.

13. W. T. Dempster, R. T. Liddicoat, “Compact Bone as a Non-Isotropic Material,” Am. J. Anat., **91** (1952).331–62

14. D.T. Reilly, A.H. Burstein, “The Mechanical Properties of CorticalBone,” *J. Bone Joint Sur.*, 57A [5] (1974)1001–1022.

15. K. Tsuda, “Studies on the Bend Strength Test and Impulsive Bending Test on Human Compact Bone,” *Journal of Kyoto Prefectural University of Medicine*., **61** (1957) 1001–25.

16. E. D. Sedlin, “A Rheological Model for Cortical Bone: A Study of the Physical Properties of Human Femoral Samples,” *Acta Orthopedica*. Scan Suppl, **83**, 1–77 (1965).

17. A. K. Dubey, K. Kakimoto, A. Obata, T. Kasuga, “Enhanced polarization of hydroxyapatite using the design concept of functionally graded materials with sodium potassium niobate,” *RSC Advances*, **4** (2014), 24601-24611.

18. V. P. Orlovskii, N. A. Zakharov, A. A. Ivanov, “Structural transition and dielectric characteristics of high purity Hydroxyapatite,” *Inorganic Materials* **32 (6)** (1996), 654-656.

---

19. M.P. Mahabole, R.C. Aiyer, C.V. Ramakrishna, B. Sreedhar, R.S. Khairnar, “Synthesis, characterization and gas sensing property of hydroxyapatite ceramic” Bulletin of Materials Science **28** (2005), 535–545.

20. D. Kumar, J. P. Gittings, I. G.Turner, C. R. Bowen, L. A. Hidalgo-Bastida, S. H. Cartmell, “Polarization of hydroxyapatite: influence on osteoblast cell proliferation” Acta Biomaterialia., **6(4)** (2010), 1549-1554

21. N. Horiuchi, M. Nakamura, A. Nagai, K. Katayama, K. Yamashita, “Proton conduction related electrical dipole and space charge polarization in hydroxyapatite,” Journal of Applied Physics., **112**, 074901 (2012).

22. N. A. Zakharov, “An analysis of the phase transitions in biocompatible $Ca_{10}(PO_4)_6(OH)_2$” *Technical physics letter* **27(12)** (2001), 1035-1037.

23. N. A. Zakharov, V. P. Orlovskii, “Dielectric characteristics of biocompatible $Ca_{10}(PO_4)_6(OH)_2$ ceramics,” *Technical physics letter*, **27(8)** (2001), 629-631.

24. T. Kijima, M. Tsutsumi, “Preparation and Thermal Properties of Dense Polycrystalline Oxyhydroxyapatite,” *Journal of the American Ceramic Society*, **62(9-10)** (1979), 455-460.

25. K. Kobayashi, M. Ryu, Y. Doshida, Y. Mizuno, C. A. Randall, “A Route Forwards to Narrow the Performance Gap between PZT and Lead-Free Piezoelectric Ceramic with Low Oxygen Partial Pressure Processed $(Na_{0.5}K_{0.5})NbO_3$,” *Journal of the American Ceramic Society* **95 [9]** (2012), 2928–2933.

26. K. K. Karkkainen, A. H. Sihvola, K. I. Nikoskinen, “Effective permittivity of mixtures: Numerical validation by the FDTD method.” IEEE Trans. Geosci. Remote Sens. **38** (2000), 1303–1308

---

27. W. D. Kingery, H. K. Bowen, D. R. Uhlmann, “Introduction to Ceramics,” Second Edition, John Wiley and Sons; (1976), 497.

28. R. E. Newnham, D. E. Skinner, L. E. Cross, “Connectivity and piezoelectric-pyroelectric composites.” *Materials Research Bulletin* **13** (1978), 525–536.

29. R. Landauer, “The electrical resistance of binary metallic mixtures.” *Journal of Applied Physics* **23** (1952), 779–784.

30. N. Jayasundere, B. V. Smith, “Dielectric constant for binary piezoelectric 0–3 composites.” *Journal of Applied Physics* **73** (1993), 2462–2466.

31. W. D Kingery, H. K. Bowen, D. R.Uhlmann, “Introduction to Ceramics,” 2nd ed. New York: Wiley Interscience, (1976), 948–949.

32. A. Laghzizil, N. El Herch, A. Bouhaouss, G. Lorente, J. Macquete, “Comparison of Electrical Properties between Fluoroapatite and Hydroxyapatite Materials,” *Journal of Solid State Chemistry.*, **156** (2001), 57-60.

33. A. Laghzizil, N. Elherch, A. Bouhaouss, G. Lorente, T. Coradin, J. Livage, “Electrical behavior of Hydroxyapatite $M_{10}(PO_4)_6(OH)_2$,” *Materials Research Bulletin.*, **36** (2001), 953-962.

34. M. Nagai, T. Nishino, “Surface conduction of porous hydroxyapatite ceramics at elevated temperatures,” *Solid State Ionics,* **28–30** (1988), 1456–1461.

35. C. Bouzidi, N. Sdiri, A. Boukhachem, H. Elhouichet, M. Ferid, “Impedance analysis of $BaMo_{1-x}W_xO_4$ ceramics,” *Superlattices Microstructure*. **82** (2015), 559–573.

36. I.M. Hodge, M.D. Ingram, A.R. West, “Impedance and Modulus Spectroscopy of polycrystalline solid electrolytes,” *Journal of Electroanalytical Chemistry,* **74** (1976), 125-143.

---

37. X. Chen, Y. Wang, J. Chen, H. Zhou, L. Fang, L. Liu, “Dielectric Properties and Impedance Analysis of $K_{0.5}Na_{0.5}NbO_3$–$Ba_2NaNb_5O_{15}$ Ceramics with Good Dielectric Temperature Stability,” *Journal of the American Ceramic Society.*, **96 [11]** (2013), 3489–3493.

38. R. Rani, S. Sharma, R. Rai, A. L. Kholkin, “Investigation of dielectric and electrical properties of Mn doped sodium potassium niobate ceramic system using impedance spectroscopy,” *Journal of Applied Physics.*, **110** (2011) 104102.

39. E. M.,Alkoy, A .Berksoy-Yavuz, “Electrical properties and impedance spectroscopy of pure and copper-oxide-added potassium sodium niobate ceramics,” *IEEE transactions on ultrasonics, ferroelectrics, and frequency control* ***59*****(10)** (2012). 2121-2128.

40. K. Das, L. Samanta, G.B.N. Chainy. “A modified spectrophotometric assay of superoxide dismutase using nitrite formation by superoxide radicals,” *Indian Journal of Biochemistry & Biophysics* **37,** (2000) 201-204.

41. C. Beauchamp, I. Fridovich, “Superoxide dismutase: improved assays and an assay applicable to acrylamide gels,” *Analytical Biochemistry,* **44 (1)** (1971) 276–287.

42. B. Chance, A. C. Maehl "[136] Assay of catalases and peroxidases," (1955): 764-775.

43. C. J. Weydert, J.J. Cullen, “Measurement of superoxide dismutase, catalase and glutathione peroxidase in cultured cells and tissue,” *nature protocols*, **5 (1)** (2010) 51-66.

44. M.H. Hadwan. “Simple spectrophotometric assay for measuring catalase activity in biological tissues,” *BMC Biochemistry*, **19 (7)** (2018).

45. R. A Greenwald, “Superoxide dismutase and catalase as therapeutic agents for human diseases. A critical review,” ISSN: 0891-5849 Free Radical Biology & Medicine., **8(2)** (1990). 210-219.

46. Y.J. Garcia, A. J. Rodríguez-Malaver, N. Peñaloza. Lipid peroxidation measurement by thiobarbituric acid assay in rat cerebellar slices, *Journal of Neuroscience Methods* **144** (2005) 127–135.

47 .J. A. Buege, S. D. Aust. “Microsomal lipid peroxidation,” *Methods in Enzymology* **52** (1978) 302-310.

48. E.D. Wills, “Lipid Peroxide Formation in Microsomes,” *Biochem. J.*, **118**(1969)315.

49. H. Ohkawa, N. Ohishiand K. Yagi, “Assay for Lipid Peroxides in Animal Tissues by Thiobarbituric Acid Reaction,” *Analytical Biochemistry*, **95**(1979)351-358.

50. L.K. Dahle, E.G. Hill, R.T. Holman, “Archives of Biochemistry and Biophysics,” **98**(1962)253-261.

51. D. Grotto et al., “Importance of the lipid peroxidation biomarkers and methodological aspects for malondialdehyde quantification,” *Química Nova*, (1), **32(**2009)169-174.

52. O.H. Lowery, N.R. Rosebrough, A.L. Farr, R.J. Randall, “Protein measurement with the folin phenol reagent,” *J Biol Chem.*, (1), **193**(1951)265-75.

53. Schaich, K. M. "Analysis of lipid and protein oxidation in fats, oils, and foods." *Oxidative stability and shelf life of foods containing oils and fats*. AOCS Press, 2016. 1-131.

54. R Sonohara , N Muramatsu , H Ohshima , T Kondo . “Difference in surface properties between Escherichia coli and Staphylococcus aureus as revealed by electrophoretic mobility measurements,” *Biophysical Chemistry (*3), **55**(1995)273-277

55. KłodzinskaE,SzumskiM, DziubakiewiczE, HrynkiewiczK, SkwarekE, JanuszW, BuszewskB, “Effect of zeta potential value on bacterial behavior during electrophoretic separation,” *Electrophoresis,* **31(**2010)1590-1596.

56. G Harkes, J Feijen, J. Dankert "Adhesion of EWerichia COD on to a series of poly(methacrylates) differing in charge and hydrophobicity," *Biomaterials,* **12**(1991)853-860.

57. A. K. Dubey, B. Basu. Pulsed electrical stimulation and surface charge induced cell growth on multistage spark plasma sintered Hydroxyapatite-Barium Titanate piezobiocomposite *Journal of the American Ceramic Society,* **97 [2]** (2014) 481–489.

58. M.P. Murphy, A. Holmgren, N.G. Larsson, B. Halliwell, C.J. Chang, B. Kalyanaraman, S.G. Rhee, P.J. Thornalley, L. Partridge, D. Gems, T. Nyström, "Unraveling the biological roles of reactive oxygen species," *Cell metabolism,* (4), **13**(2011)361-366.

59. X.Q. Chen, X.Z. Tian, I. Shin, J. Yoon, "Fluorescent and Luminescent Probes for Detection of Reactive Oxygen and Nitrogen Species," *Chemical Society Reviews* (9), **40**(2011)4783−4804.

60. D. Kumar , J.P. Gittings, I.G. Turner, C.R. Bowen, L.A. Hidalgo-Bastida, S.H. Cartmell, "Polarization of hydroxyapatite: Influence on osteoblast cell proliferation," *Acta Biomaterialia*, **6**(2010)1549-1554.

61. S. Itoh, S. Nakamura, M. Nakamura, K. Shinomiyaa, K. Yamashita, "Enhanced bone ingrowth into hydroxyapatite with interconnected pores by electrical polarization," *Biomaterials,* **27** (2006) 5572-5579.

62. S. Nakamura, T. Kobayashi, K. Yamashita, "Extended bioactivity in the proximity of hydroxyapatite ceramic surfaces induced by polarization charges," *Journal of Biomedical Materials Research* **61**(2002)593-599.

63. S. Itoh, S. Nakamura, T. Kobayashi, K. Shinomiya, K. Yamashita, "Effect of electrical polarization of hydroxyapatite ceramics on new bone formation," *Calcified Tissue International* **78**(2006)133-42.

---

64. S. Itoh, S. Nakamura, M. Nakamura, K. Shinomiya, K. Yamashita, “Enhanced bone regeneration by electrical polarization of hydroxyapatite,” *Artif Organs,* **3**(2006)863-9.

65. S. Itoh, S. Nakamura, M. Nakamura, K. Shinomiyaa, K. Yamashita, “Enhanced bone ingrowth into hydroxyapatite with interconnected pores by electrical polarization,” *Biomaterials,* **27**(2006)5572-5579.

66. T. Kobayashi, S. Nakamura, K. Yamashita, “Enhanced osteobonding by negative surface charges of electrically polarized hydroxyapatite,” *Journal of Biomedical Materials Research,* **57**(2001)477-484.

67. N.C. Teng, S. Nakamura, Y. Takagi, Y. Yamashita, M. Ohgaki, K. Yamashita, “A new approach to enhancement of bone formation using electrically polarized hydroxyapatite,” *Journal of Dental Research,* **80**(2001)1925-1292.

68. S. Nakamura, T. Kobayashi, K. Yamashita, “Numerical osteobonding evaluation of electrically polarized hydroxyapatite ceramics,” *Journal of Biomedical Materials Research A,* **68**(2004)90-94.

69. M. Ohgaki, T. Kizuki, M. Katsura, K. Yamashita, “Manipulation of selective cell adhesion and growth by surface charges of electrically polarized hydroxyapatite,” *Journal of Biomedical Materials Research* **57** (2001)366-373.

70. A.K. Dubey, S.D. Gupta, B. Basu, “Optimization of electrical stimulation parameters for enhanced cell proliferation on biomaterial surfaces,” *Journal of Biomedical Materials Research Part B: Applied Biomaterial,* **8B** (2011)18-29.

71. J. Tong, L. Sun, B. Zhu, Y. Fan, X. Ma, L. Yu, J. Zhang, “Pulsed electromagnetic fields promote the proliferation and differentiation of osteoblasts by reinforcing intracellular calcium transients,” *Bioelectromagnetics,* **38** (2017) 541-549.

72. M.Zhai, D. Jing, S. Tong, Y. Wu, P. Wang, Z. Zeng, G. Shen, X. Wang, Q. Xu, E. Luo, "Pulsed electromagnetic fields promote in-vitro osteoblastogenesis through aWnt/b-Catenin signaling-associated mechanism," *Bioelectromagnetics*, **37**(2016)152-162.

73. P. Zhou, F. He, Y. Han, B. Liu, S. Wei, "Nanosecond pulsed electric field induces calcium mobilization in osteoblasts," *Bioelectrochemistry*, **124**(2018)7-12.

74. M.R. Love, S. Palee, S.C. Chattipakorn, N. Chattipakorn, "Effects of electrical stimulation on cell proliferation andapoptosis," *Journal of Cellular Physiology*, **233**(2018)1860-1876.

75. M. Nakamura, A. Nagai, A. Hentunen, J. Salonen, Y. Sekijima, T. Okura, K. Hashimoto, Y. Toda, H. Monma, K. Yamashita, "Surface Electric Fields Increase Osteoblast Adhesion through Improved Wettability on Hydroxyapatite Electret," *ACS applied materials & interfaces*, **(10) 1** (2009)2181-2189